THESIS FOR THE DEGREE OF DOCTOR OF PHILOSOPHY

Tuned acidity in zeotypes

A descriptor to unravel the direct conversion of methane to methanol

Simone Creci

CHALMERS

Department of Chemistry and Chemical Engineering
CHALMERS UNIVERSITY OF TECHNOLOGY
Göteborg, Sweden 2020

Tuned acidity in zeotypes

A descriptor to unravel the direct conversion of methane to methanol

Simone Creci

ISBN 978-91-7905-422-9

© Simone Creci, 2020.

Doktorsavhandlingar vid Chalmers tekniska högskola

Ny serie Nr. 4889

ISSN 0346-718X

Department of Chemistry and Chemical Engineering
Chalmers University of Technology
SE-412 96 Göteborg
Sweden
Telephone +46 31 772 1000

Cover:
Image of a heart-shaped crystal of one of the samples investigated in this work. My relationship with these materials has not been all roses, but can be perfectly summarized by Catullus' quote "*Odi et amo. Quare id faciam fortasse requiris. Nescio, sed fieri sentio et excrucior.*"

Typeset in LaTeX using the kaobook class
Printed by Chalmers Reproservice
Göteborg, Sweden 2020

Tuned acidity in zeotypes
A descriptor to unravel the direct conversion of methane to methanol

Simone Creci
Department of Chemistry and Chemical Engineering
Chalmers University of Technology

Abstract

The catalyst's acidity is crucial in countless chemical reactions, and to tune this parameter means to take the lead on the desired catalytic reaction. Therefore, it is not surprising that zeolites have been used since decades as catalysts for their outstanding properties of solid acids. Alongside, zeotypes are zeolite-like materials whose chemical composition is altered to obtain *ad hoc* acidity, and are therefore of outmost interest for many catalytic reactions. Here, the chosen reaction affected by the zeotype acidity is the direct conversion of methane to methanol. Indeed, a lower acidity of the zeotype promotes the extraction of methanol, whose precursors tend to remain adsorbed on the acidic sites of the zeotype.

In this study, Al, B, Fe, Ga, and Ti are incorporated in the MFI framework of silicalite zeotypes. The zeotype crystallites are imaged with scanning and transmission electron microscopy, and the MFI framework structure is characterized with X-ray diffraction, nitrogen sorption and Raman spectroscopy. The process from the as synthesized samples to the corresponding materials in the acid form is examined with *in situ* infrared spectroscopy, with and without ammonia and nitric oxide as probe molecules. Furthermore, the following series of increasing acidity is observed by means of infrared spectroscopy: 0 = pure silicalite = Ti-silicalite < B-silicalite < Fe-silicalite < Ga-silicalite < Al-silicalite.

The influence of the zeotype acidity during methane exposure and temperature programmed desorption of methanol has been investigated *in situ* with infrared spectroscopy. The results show that the presence of iron promotes methane activation and that methanol is more strongly bound to the zeotype in the presence of stronger acid sites. Because methane activation and methanol extraction are two of the key steps in the direct conversion of methane to methanol, our results indicate that Al-free zeotypes with tuned acidity pinpoint important catalyst design parameters needed for this reaction.

Keywords: zeolite, zeotype, infrared spectroscopy, MFI, methane, methanol, catalysis

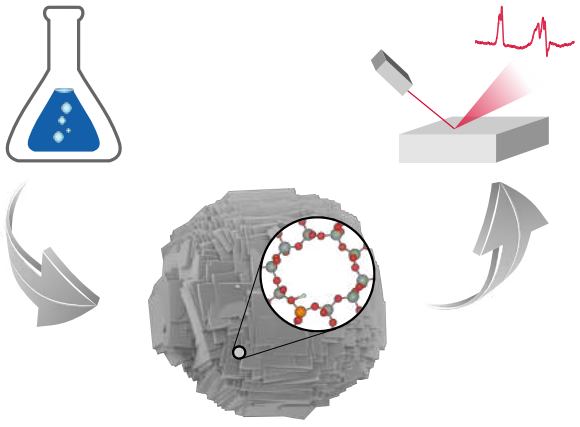

List of Publications

This thesis is based on the following appended papers:

I. Tuned Acidity for Catalytic Reactions: Synthesis and Characterization of Fe- and Al-MFI Zeotypes

S. Creci, X. Wang, P-.A. Carlsson and M. Skoglundh

Topics in Catalysis, 62 **(2019)**, 689-698

II. Local anisotropy in single crystals of zeotypes with the MFI framework structure evidenced by polarised Raman spectroscopy

A. Martinelli, S. Creci, S. Vavra, P-.A. Carlsson and M. Skoglundh

Physical Chemistry Chemical Physics, 3 **(2020)**, 1640-1654

III. Methoxy ad-species in MFI zeotypes during methane exposure and methanol desorption followed by *in situ* IR spectroscopy

S. Creci, X. Wang, P-.A. Carlsson, A. Martinelli and M. Skoglundh

Accepted for publication in *Catalysis Today* **(2020)**

IV. Acidity as descriptor for methanol desorption in B-, Ga- and Ti-MFI zeotypes

S. Creci, A. Martinelli, S. Vavra, P-.A. Carlsson and M. Skoglundh

Manuscript

My Contributions to the Publications

Paper I

I prepared the zeotype samples, performed all experimental work and data analysis, interpreted the results with the help of the co-authors and wrote the first draft of the manuscript. I was responsible for the writing process, the manuscript submission and the answering of the reviewers' comments on the manuscript.

Paper II

I prepared the zeotype samples, followed the data analysis and contributed to write the manuscript and to answer the reviewers' comments on the manuscript.

Paper III

I prepared the zeotype samples, performed all experimental work (except the SEM images) and data analysis, interpreted the results with the help of the co-authors and wrote the first draft of the manuscript. I was responsible for the writing process, the manuscript submission and the answering of the reviewers' comments on the manuscript.

Paper IV

I prepared the zeotype samples, performed all experimental work (except the SEM images) and data analysis, interpreted the results with the help of the co-authors and wrote the first draft of the manuscript. I was responsible for the writing process, the manuscript submission and the answering of the reviewers' comments on the manuscript.

Dear, Liebe, Cari...

... Magnus,

You have given me essential help during my doctoral studies and cheered me up even in the darkest moments

... Anna and Per-Anders,

You have supported me in my research and shared your knowledge throughout the past five years

... David, Felix and Ting,

Not only you have always showed me extreme patience in the lab, but you have also proved to be true friends.

... LL, Chris, Johanna, Lars, Milene, Peter and Saba,

The memories of my studies and especially of our beloved kitchen will be fabulous also thanks to you

... Papà,

Gli insegnamenti che mi hai dato sin da grande ero piccolo non verranno mai dimenticati.

... Carmen, Federica e Giulio,

Questi cinque anni nelle fredde Terre Scandinave avevano proprio bisogno di un po' del vostro calore italico.

... Draghi, Gianni e Nick,

Mai siete stati più lontani, eppure mai vi ho sentiti così vicini, ci sarà sempre uno spazio per voi vicino a me.

... Nonni,

Questo è anche frutto del vostro amore, e mai mi ne dimenticherò.

... Mima,

Sei il primo esempio di forza e coraggio, e sono onorato ed orgoglioso d'essere tuo figlio: mai ce l'avrei fatta senza di te!

and Martina,

du bist die Sonne, die mich jeden Tag erleuchtet, die Sonne, die mir Kraft gibt, wenn alles verloren scheint. Ich freue mich sehr zu sehen, welche Pläne das Leben für uns hat, und gemeinsam weiß ich, dass es eine fantastische Reise werden wird!

... Thanks, Danke, Grazie!

Simone, December 2020

Contents

Abbreviations and acronyms

BAS	Brønsted acid site
BET	Brunauer-Emmett-Teller
DCMM	Direct conversion of methane to methanol
DRIFTS	Diffuse reflectance infrared Fourier transform spectroscopy
Fe_{ex}-*Me*-S	Fe-exchanged silicalite sample with metal *Me* incorporated in the MFI framework
Fe-*extra*	Iron species in extra-framework position
IR	Infrared
Me-BAS	Brønsted acid site generated by the metal *Me* in the MFI framework
Me-S	Silicalite sample with metal *Me* incorporated in the MFI framework
n-MR	*n*-membered ring
SAR	Silicon-to-aluminum ratio
SDA	Structure directing agent
SEM	Scanning electron microscopy
SSA	Specific surface area
TEM	Transmission electron microscopy
TEOS	Tetraethyl orthosilicate
TPA	Tetrapropylammonium
TPD	Temperature programmed desorption
XRD	X-ray diffraction

List of Figures

Introduction 1

Rön och beskrifning om en obekant bärg art, som kallas Zeolites.
(Finding and describing an unknown rock type, called Zeolites.)

Axel Fredrik Cronstedt, 1722-1765

Figure 1.1: Axel Fredrik Cronstedt (1722-1765).

It was the year 1756 when the Swedish mineralogist Axel Fredrik Cronstedt named a class of minerals *Zeolites* [1]. After him, many scientists intensively investigated the unique properties of zeolite minerals, but only in 1862 the first artificial zeolite was synthesized by St. Claire Deville by hydrothermal crystallization [2]. This event signed the start of a tremendous research on new zeolite structures and an intense exploration of their applications. Remarkable was when in 1954 synthetic zeolites were commercialized by Union Carbide as a new class of industrial materials [3]. The *acme* in the field of zeolites synthesis was reached in the 1980's and the 1990's when more then 100 new zeolite structures were artificially prepared [4]. From 1756 to now, zeolites have found applications in countless fields, for example in heterogeneous catalysis.

The direct conversion of methane to methanol, DCMM, has been appointed as the "Holy Grail"[5] for catalysis or as the "Dream Reaction"[6] of the last two decades. [1] In nature, some enzymes, particularly the methane monooxygenases (MMO), are known to selectively convert methane to methanol, although with low conversion rates [8]. In light of these facts, I was not surprised in learning from the literature that the study of such a complex and challenging reaction as the DCMM could take large advantage of the outstanding properties of zeolites. Indeed, it happens that zeolites, among their various properties, show sites similar to the active sites in the MMO enzymes. Therefore, zeolites used as heterogeneous catalysts have been intensively studied for the DCMM and represent nowadays one of the most promising candidates to unriddle this reaction.

1: Currently, methanol is produced in massive facilities *via* syngas in a two stages process, using high temperatures and pressures. Therefore, the DCMM at low temperature and low pressure is desirable both from an energy and sustainability perspective. The breakage of the strong C – H bond in the methane molecule and the easy over-oxidation of methanol represent the main thermodynamic challenges in the DCMM [7].

Methane activation and methanol extraction seem to be the limiting steps when both high methane conversion and high selectivity towards methanol are pursued. In particular, the acidity of the zeolite is considered a crucial descriptor in the DCMM. In this perspective, the challenge is to design zeolite-like materials, called *zeotypes*, with *ad hoc* acidity capable both to dissociatevely adsorb methane and to easily desorb methanol on and from the catalyst internal surface. Therefore, it is of major importance to control the material synthesis and to understand the resulting properties to be able to maximize the catalyst performances.

The objective of this PhD thesis project is to investigate the chemical and physical properties of synthesized zeotype samples to benefit the fundamental understanding of the direct conversion of methane to methanol. The analysis is focused on the materials properties and on how these might influence the DCMM. Particular attention is given to the study of the zeotype acidity and on how this affects the two key steps of methane activation and methanol extraction in the direct conversion of methane to methanol.

1.1 Tips for a smooth navigation of this thesis

Structure of the manuscript This thesis is divided in Chapters which in turns are divided in Sections and sub-Sections. On the top-left of even pages and on the top-right of odd pages you can find the titles of the relative Chapter and Section, respectively.

Side column The use for the main text of a column narrower than the page width allows the use of a side-column where notes, figures and tables are reported. [2]

2: Example of sidenote.

Abbreviations A list of the abbreviations used in this thesis is reported on Page III.

List of Figures A list of all figures shown in this thesis is reported on Page V.

Take-home messages Each Section is followed by a *Take-home message*, presented in a blue box, where a short summary of the Section is reported.

The samples In Figure 3.7 a summary of all investigated samples together with the performed experiments and the relative Section is reported. A good way to find back the right way if you get lost while reading!

Take-home message

In this thesis zeotypes with tuned acidity are investigated with an eye on their application as catalysts in the direct conversion of methane to methanol. This work is the result of the past four years of my doctoral studies, where the most relevant results are reported and discussed. I wish you a pleasant and enjoyable reading!

Background 2

2.1 *Zeo*-materials and their characteristics

Zeolites: extraordinary materials for endless applications

The word *zeolite* was coined by the Swedish mineralogist Axel Fredrik Cronstedt in 1756 to describe a particular class of minerals capable of adsorbing water and releasing it as vapor by increasing the temperature [1]. Indeed, *zeolite* literally means 'boiling stone' from the greek $\zeta\acute{\epsilon}\omega$ (=to boil) and $\lambda\acute{\iota}\theta o\varsigma$ (=stone). In Figure 2.1 an image of Stilbite-Ca-Natrolite-Laumontite zeolite is shown.

Zeolites are hydrated porous tecto-aluminosilicate minerals which occur naturally in large amounts. China is the biggest producer of zeolites with around 2000 thousands tons produced in 2008, followed by Jordan, The Republic of Korea and Japan [9]. In nature, there exist about 56 different types of zeolites, but nowadays more than 150 additional types have been synthesized [10]. The majority of the zeolite industry is focused in producing detergents for removing calcium ions as ion-exchangers. Nevertheless, zeolites are also widely used for their properties of molecular sieves (*e.g.* for gas separation in air) and in the catalysis field for their high surface area, their acidic properties and their capability to host metals in ion-exchange position. Fluid catalytic cracking (FCC) is an example which uses large amounts of zeolites [11].

Figure 2.1: Example of mineral zeolite (Stilbite-Ca-Natrolite-Laumontite). This file is licensed under the Creative Commons Attribution-Share Alike 3.0 Unported license. Attribution: Rob Lavinsky, iRocks.com – CC-BY-SA-3.0

Zeotypes: the isomorphous substitution of Si with Me^{3+} and Me^{4+}

The primary unit of the zeolite structure is the SiO_4^{4-} tetrahedron. The collection of primary units builds up secondary units which in turn build up the framework structure. The presence of Al^{3+} in place of Si^{4+} in the framework structure induces a net negative charge in the zeolite which is balanced by a counter cation [1]. When the counter cation is H^+, the $\equiv Si^{4+}-O(H^+)-Al^{3+}\equiv$ sequence is called Brønsted acid site, BAS (see Figure 2.2). Upon dehydration, *e.g.* by increasing the temperature, the BAS loses the $-OH$ group and gives rise to a Lewis acid site. [2]

One of the most significant properties of zeolites is thus to behave as solid acids by donating the proton of the BASs [14]. One can tune the amount of BASs by changing the amount of Al in the

1: *e.g.* Na^+, NH_4^+, H^+, Fe^{3+}, *etc.*

2: It is clear that by increasing the amount of Al one can increase the amount of BASs, although the Loewenstein's rule forbids the presence of an $\equiv Al-O-Al\equiv$ linkage in the structure [12]. Therefore, the lowest allowed Si to Al molar ratio, SAR, is 1.

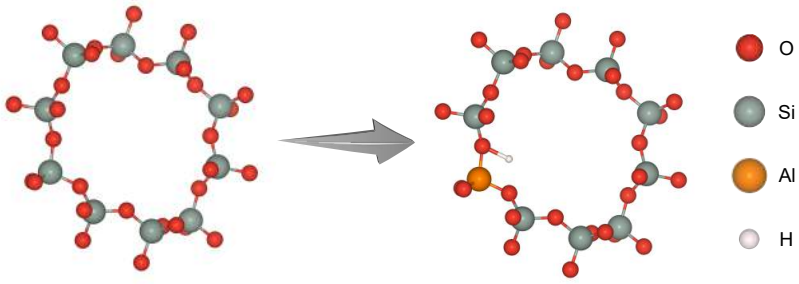

Figure 2.2: Schematic representation of the isomorphous substitution of Si with Al in the zeolite framework, and consequent formation of the Brønsted acid site. Drawing produced by Vesta [13].

framework, but for a given type of framework structure, the acidity strength of the BASs may not be influenced by the Si/Al ratio [15]. In this perspective, elements with oxidation state +3 other than Al [3] have been incorporated in framework position to control the acidity strength [16–19]. [4] The term *zeotype* will be used in this work to address these microporous materials showing typical zeolite structures but having various elements incorporated in framework positions. [5]

The MFI framework

The TO_4^{4-} tethraedrons [6] in zeotypes are assembled together forming channels and cages, which in turn form the overall framework structure. There exist more than 200 types of frameworks, and they are all labeled with a 3-letters code. In this work, all samples show the framework structure schematically represented in Figure 2.3, labeled as MFI. This structure is characterized by 10-, 6- and 5-membered rings (MR) and by the presence of channels and no cages. [7] The 10-MR windows define two intersecting systems of channels: one composed by parallel straight channels and one composed by zig-zag channels orthogonal to the first ones. When composed only by Si and O, the material is called silicalite [21]. When also Al is present, the commercial name is ZSM-5. [8]

Take-home message

Zeolites are microporous aluminosilicates whose primary building blocks are SiO_4^{4-} tethraedrons. When an element with oxidation state +3 is incorporated in the zeolitic framework in place of Si, a counter cation is needed to balance the net negative charge. Brønsted acid sites are generated when the counter cation is a H^+ ion. Different elements incorporated in place of Si will therefore generate Brønsted acid sites with different acidity strength.

3: *e.g.* B, Fe, Ga, *etc*.

4: The incorporation of elements with oxidation state +4 (*e.g.* Ti) is not expected to form Brønsted acidity as no negative charges are induced in the framework.

5: Furthermore, the term Brønsted acid site will be used also for the acid sites generated by metals other than Al in framework position.

6: where T = Si or the metal incorporated in the framework.

7: The 10-MRs windows are about 5.5 Å in diameter. The average Si–O distance is 1.57-1.62 Å and and the average O–Si–O angle is 107.9° [20].

8: For clarity, in this work all samples will be referred as silicalite.

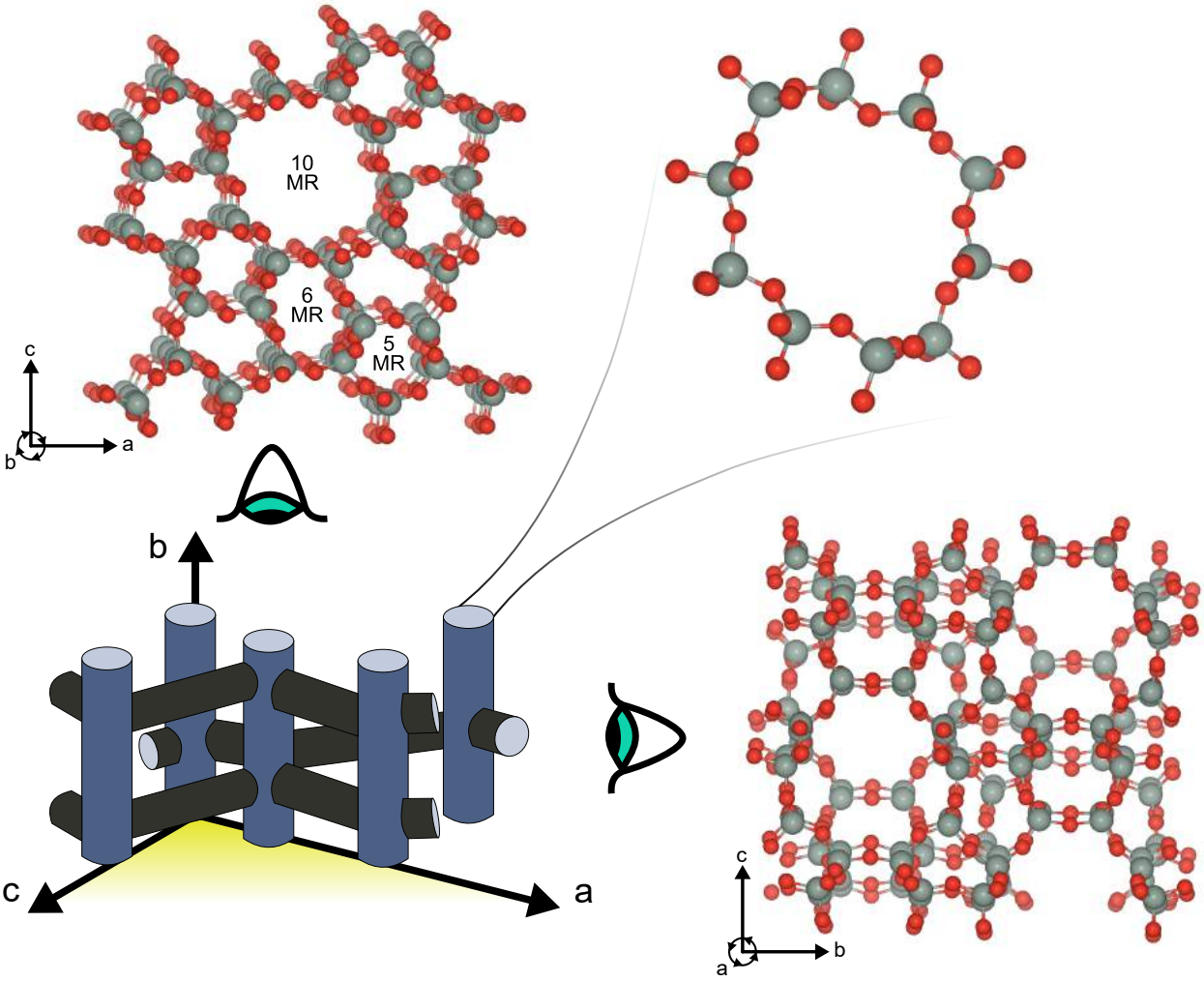

Figure 2.3: Schematic representations of the MFI type of framework. Drawing produced by Vesta [13].

2.2 Synthesis of zeotypes

The presence of impurities in the natural zeolite minerals and the need of new framework structures have been the driving forces in the field of zeotype synthesis. Furthermore, Al-free zeotypes can not be found in nature and appropriate synthesis procedures must be followed depending on the metal added in place of Si. In this Section, I will focus on the synthesis by the sol-gel method followed by hydrothermal crystallization of MFI silicalite zeotypes as they are the materials investigated in this work.

Choice of the chemicals used for the synthesis

In a standard zeotype synthesis, the ingredients are:

- silica source;
- structure directing agent (SDA);
- metal precursors;
- water;
- pH control agents.

Low-molecular-weight silica sources (*e.g.* tetraethyl orthosilicate, TEOS) are usually preferred as they produce more primary units (SiO_4^{4-}) when dissolved in water and thus they promote the formation of the metallosilicate network in the gel [22]. [9] Furthermore, when TEOS is used as silica source, nucleation and crystal growth occur more rapidly than when a high-molecular-weight silica source is used [23]. TEOS also provides high purity SiO_4^{4-} tetrahedrons after hydrolysis and condensation processes at appropriate pH values and stirring times [24].

9: When high-molecular-weight silica sources (*e.g.* fumed silica) are used, metal complexes tend to form on the external surface of the silica source.

The structure directing agent, SDA, is usually an organic molecule and defines the zeotype framework structure by directing the crystallization process. [10] The most used SDA for the MFI framework is the tetrapropylammonium ion, TPA^+, in hydroxide or salt form, *e.g.* bromide. [11] A schematic representation of the TEOS molecule and the TPA^+ ion is shown in Figure 2.4.

10: It is important to stress that the SDA is not only an organic template, as it actively controls the way the metallosilicate network ordinates in the gel during crystallization [25].

11: TPA^+ is the only homoleptic tetraalkyl ammonium molecule, showing four identical propyl chains symmetrically distributed in the space around the N atom.

The type of metal precursor does not significantly influence the synthesis procedure. Usually, metal complexes like nitrates are used as they easily dissolve in water. High-purity water, *e.g.* Milli-Q water, is recommended to avoid the presence of impurities in the zeotype framework. The pH control agents should not severely interact with the crystallization process. [12]

12: However it has been shown that the presence of Na^+ ions increases the nucleation rate by increasing the rate of dissolution of the silica source [26].

From the synthesis gel to the zeotype crystals

A schematic representation of the synthesis from the sol-gel preparation to the formation of the zeotype samples in the final form is shown in Figure 2.5. The first step is the dissolution of the silica source and the metal precursors in water in order to obtain the

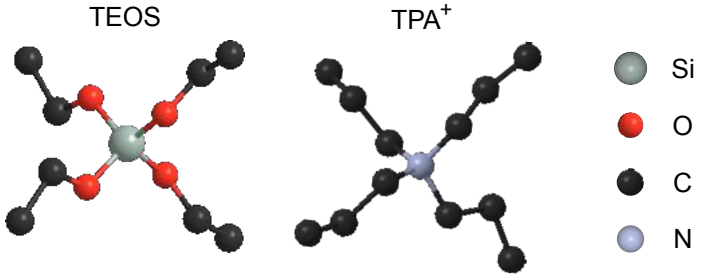

Figure 2.4: Schematic representation of the TEOS molecule and the TPA^+ ion.

SiO_4^{4-} primary units and the metal ions, respectively. [13] Chains and then networks of metallosilicates species form in this first solution. In a second solution, the TPA^+ ions are dissolved in water. During this step, the water molecules reorganize around the propyl chains by hydrophobic hydration of the TPA^+ ions.

The TPA^+-solution is then added to the metallosilicate solution. [14] As soon as the TPA^+ ions get in contact with the metallosilicate network, Van der Waals or hydrophobic interactions arise between the two species and the liquid solution becomes a sol. [15] Once the TPA^+-solution is completely added to the metallosilicate solution, the pH is increased to 10-11 to promote the crystallization process. The viscosity of the sol increases and the so obtained gel is transferred to an autoclave.

The hydrothermal crystallization takes place in autoclaves, where the high pressure allows the silicate network to nucleate and grow around the TPA^+ ions. [16] During crystallization, it has been shown that the TPA^+ ions do not simply act as space-filling agents, rather they rearrange the metallosilicate network in the final framework structure. An organic-inorganic composite forms where each TPA^+ ion involves 24 SiO_2 units and locates itself at the 10 MR channels intersections of the MFI structure. [17]

After crystallization, the TPA^+ ions are tightly enclatrated in the zeotype channels and do not show the spacial symmetry of the free TPA^+ ions in the TPA^+-solution previously prepared. The so obtained zeotype crystals are washed with Milli-Q water, filtered and freeze-dried overnight, and the organic molecule is removed by calcination in air. [18] The NH_4^+-form of zeotype samples is achieved by NH_4^+-exchange of the zeotype samples in the Na^+-form. [19] A second calcination at 500 °C for 5 h starting from room temperature with a heating ramp of 5 °C min^{-1} is performed to decompose the ammonium ions and therefore to obtain the H^+-form of the zeotype samples.

Challenges in the synthesis of Al-free zeotypes

The isomorphous substitution of Si^{4+} with Al^{3+} in zeolites has been intensively studied in the literature [30–32]. It is well established that the similar electronic configuration and ionic dimensions, and the stability of the oxidation state of Al^{3+} allow minor alterations in the framework structure when Al is in framework position. Indeed, it is not surprising that natural zeolites are composed by Si and Al. Ge^{4+} was the first cation isomorphically substituted in a zeotype structure [33], but afterwards many tri-, tetra- and pentavalent cations have been added during synthesis to partially substitute Si^{4+} in framework position.

13: Several factors might influence this first step (stirring time, temperature, concentration, *etc.*), but the pH of the solution must be carefully controlled to avoid precipitation of insoluble metal species.

14: The reverse addition is less effective as precipitation of metal species may occur for higher amounts of metal [27].

15: The propyl chains interact preferentially with the hydrophobic silicate species rather than with the bulk H_2O molecule [28].

16: The reaction time and the temperature at which the hydrothermal crystallization is performed depend on the zeotype. For the zeotypes synthesized in this work, 5 days and 170 °C were chosen according to literature [27].

17: In particular, two of the four propyl chains of the TPA^+ ions are believed to extend in the straight channels and two in the zig-zag channels [29].

18: Several parameters can be found in the literature about the calcination of the as synthesized samples. In this work, the SDA-containing samples were calcined at 500 °C for 5 h starting from room temperature with a heating ramp of 5 °C min^{-1}.

19: After calcination of the SDA-zeotype samples, the counter cations which balance the framework discharges are likely the Na^+ ions used during the sol-gel preparation as pH control agent.

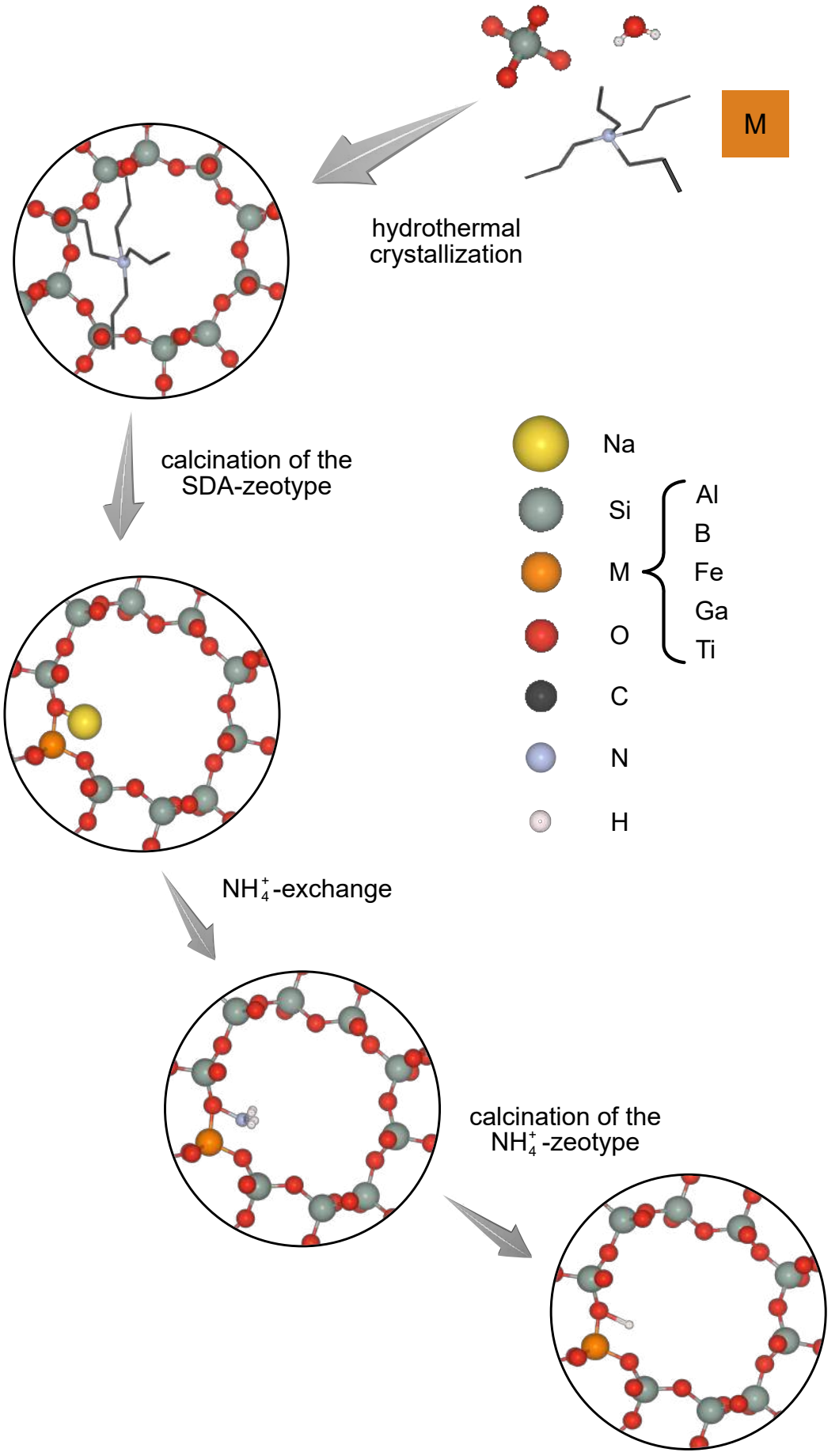

Figure 2.5: Schematic representation of the synthesis steps from the sol-gel preparation to the formation of the zeotype samples in the final form. Drawing produced by Vesta.[13]

The challenges in the isomorphous substitution of Si^{4+} with Me^{3+} in zeotype structures consist in the difference of the ionic radii and the ability of some metals to change oxidation state. [20] These two factors make the crystal structure of the zeotype less stable than the crystal structure of the parent zeolite.

Another reason why the addition of metals other than Al is difficult concerns the synthesis procedure. As described above, the most common zeolite and zeotype synthesis method consists in preparing a gel which further crystallizes in a basic environment. Some metals tend to form unwanted species in the basic environment necessary for the crystallization [21] and therefore, the metal precursors must be added at appropriate pH conditions. Only once the metallosilicate network is formed, the pH can be increased to the basic conditions necessary for the crystallization. [22]

Take-home message

One way of preparing *zeo*-materials consists of the sol-gel method followed by hydrothermal crystallization in autoclave. The incorporation of Al in zeolites is facile. On contrary, *ad hoc* ingredients and synthesis parameters shall be chosen to obtain zeotypes with the desired framework structure and to successfully incorporate the metal in the framework.

20: For example, the crystal ionic radii of Si^{4+} and Fe^{3+} are 54 and 78 pm, respectively, and Fe^{3+} easily changes oxidation state to +2.

21: For example, Fe tends to precipitate as ferric hydroxide at pH higher than 4 [34] and therefore it must be added to the sol in acid conditions.

22: In zeolites synthesis, minor precautions are needed when the Al precursor is added to the sol as it does not tend to form unwanted species in the basic environment necessary for the crystallization.

2.3 The direct conversion of methane to methanol

Why methane and why methanol?

Methane [23] is the main component of natural gas, followed by other higher alkanes (mostly ethane, propane and butane), carbon dioxide, nitrogen and hydrogen sulfides. In turn, natural gas is highly abundant on earth. In 2014, almost 200 trillion cubic meters of natural gas have been globally produced, with China leading with around 18 trillion cubic meters [36]. Furthermore, although methane has a 28 times stronger global warming potential (GWP) than CO_2, it is considered a promising alternative to crude oil as green feed stock for the chemical and fuel industry [37].

Methanol [24] is extensively used both as chemical alone and as primary source for the synthesis of chemicals based on longer carbon chains, aromatics and hydrocarbons. Methanol also represents a promising fuel. Indeed, its liquid state at room conditions makes it easier to store than other alternative feed stocks to crude oil, *e.g.* methane or hydrogen, and it shows relatively high energy density

23: Methane is a tethraedral molecule composed by four identical C−H bonds. Its chemical formula is CH_4 and its molar mass is 16.04 g mol^{-1}. At room temperature and atmospheric pressure it is an odorless and colorless gas. In nature, methane is formed both in thermogenic and abiotic processes (*i.e.* organic and inorganic), and by enzymes in the methanogenesis process [35].

24: Methanol is the simplest alcohol composed by a methyl group bonded to a hydroxyl group. Its chemical formula is CH_3OH and its molar mass is 32.04 g mol^{-1}. At room temperature and pressure it is a colorless, flammable and volatile liquid. It is easily biodegradable and miscible in water [38]. In nature, it is produced in the anaerobic metabolism of some bacteria and is present in small quantities both in the environment and in the human body [39].

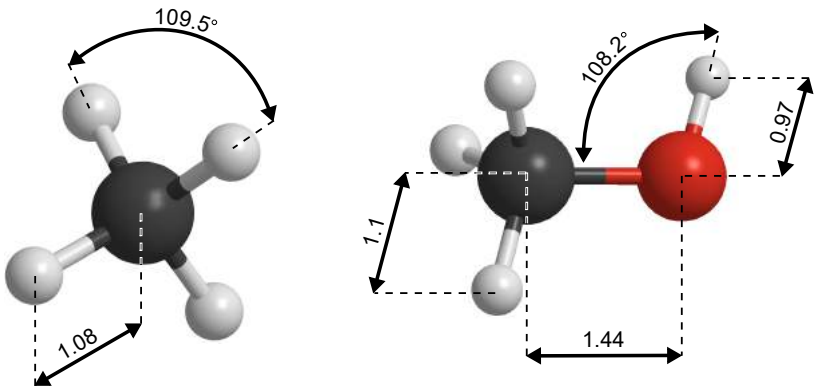

Figure 2.6: Molecular structures of methane and methanol (all bond distances are shown in Å).

[40]. A schematic representation of the methane and the methanol molecules is shown in Figure 2.6 .

Challenges in the one-step reaction

Nowadays, methanol is industrially produced from methane in a multi-stage process which involves first the formation of syngas from methane at high temperature and then the liquefaction to methanol at high pressures. This process involves massive industrial plants and is energy intense and costly. Therefore, the partial oxidation of methane to methanol at lower temperatures and pressures is desired from energy, sustainability and economic perspectives [7]. [25]

The main challenges in the direct conversion of CH_4 to CH_3OH, DCMM, consist in activating CH_4 and avoiding the over-oxidation of CH_3OH. Indeed, methane is the most stable hydrocarbon existing in nature and, therefore, high amount of energy is required for its activation. [26] Furthermore, CH_4 tends to form oxides more stable than methanol, mostly CO_2, when exposed to oxidizing environment. Thus the goal is to provide a method severe enough to dissociate the CH_4 molecule and simultaneously mild enough to prevent the CH_3OH molecule to further oxidize.

Zeolites as catalysts for the direct conversion of methane to methanol

One of the most promising technologies investigated in literature for the DCMM involves zeolites used as heterogeneous catalysts. The procedure usually involves four steps (a schematic representation of this procedure is shown in Figure 2.7).

1. **Catalyst preparation** Metals are added to the zeolite by different methods. [27] Scanning the literature, Fe- and Cu-containing MFI zeolites seem to be one of the most promising catalysts

25: Several technologies have been investigated to directly convert CH_4 to CH_3OH, which involve gas-phase reactions, heterogeneous, bio- and photo-catalysis, plasma technology and membrane technology [41]. Nevertheless, none of these methods has shown appreciable results for possible commercialization both in terms of high activity and high selectivity towards CH_3OH.

26: For alkanes, the dissociation energy required to cleave the first C–H bond is highest for methane (439 kJ mol^{-1}) but not very much higher compared to *e.g.* ethane (423 kJ mol^{-1}). Abstraction of the first hydrogen from ethene (457 kJ mol^{-1}) and benzene (551 kJ mol^{-1}) is higher, despite these compounds are more easy to activate than methane [42]. Methane is a molecule with four sp^3 hybridized orbitals from carbon, filled with one electron each, forming four bonding molecular orbitals with one s electron from each hydrogen. The methane molecule is therefore rather stable. So the activation depends on the electron structure of the entire molecule and not only on the C–H bond strength.

27: For example, both zeolites and zeotypes can host metals in ion-exchange position in place of the H^+ belonging to the BASs. In the case of zeotypes containing only Si and O, metals can be added by incipient wetness impregnation methods, forming metal clusters inside the pores and on the external surface of the catalyst. Metals can also be added in framework position as previously discussed.

for the DCMM. However, the structure of the active sites is still under debate [37].

2. **Catalyst activation** Before being exposed to methane, the catalyst often needs to be activated at high temperature in oxidizing environment, *e.g.* O_2, N_2O or NO. [28]
3. **Methane activation** Once the active site is formed, the catalyst is exposed to CH_4, usually at around 200-250 °C to promote the adsorption of the molecule. Depending on the active site and the support material, methane is dissociatevely adsorbed and oxidized on the active sites on the catalyst surface by cleavage of one C–H bond of the molecule. Therefore the aim is to adsorb CH_4 as methoxy groups and avoid their overoxidation [45–47].
4. **Methanol extraction** It has been shown that after methane is activated on the surface, most of the reaction products remain adsorbed on adsorption sites [48]. The extraction of methanol by use of solvents, *e.g.* water, and/or increasing the catalyst temperature is thus a necessary step in the DCMM for appreciable amounts of the desired product.

28: For example, in the case of Fe, a pretreatment at 250 °C in N_2O allows the formation of highly reactive sites in extra-framework position [43]. These highly reactive sites have been shown in the literature to be able to activate methane in the zeolite and have therefore been intensively studied for the DCMM [44].

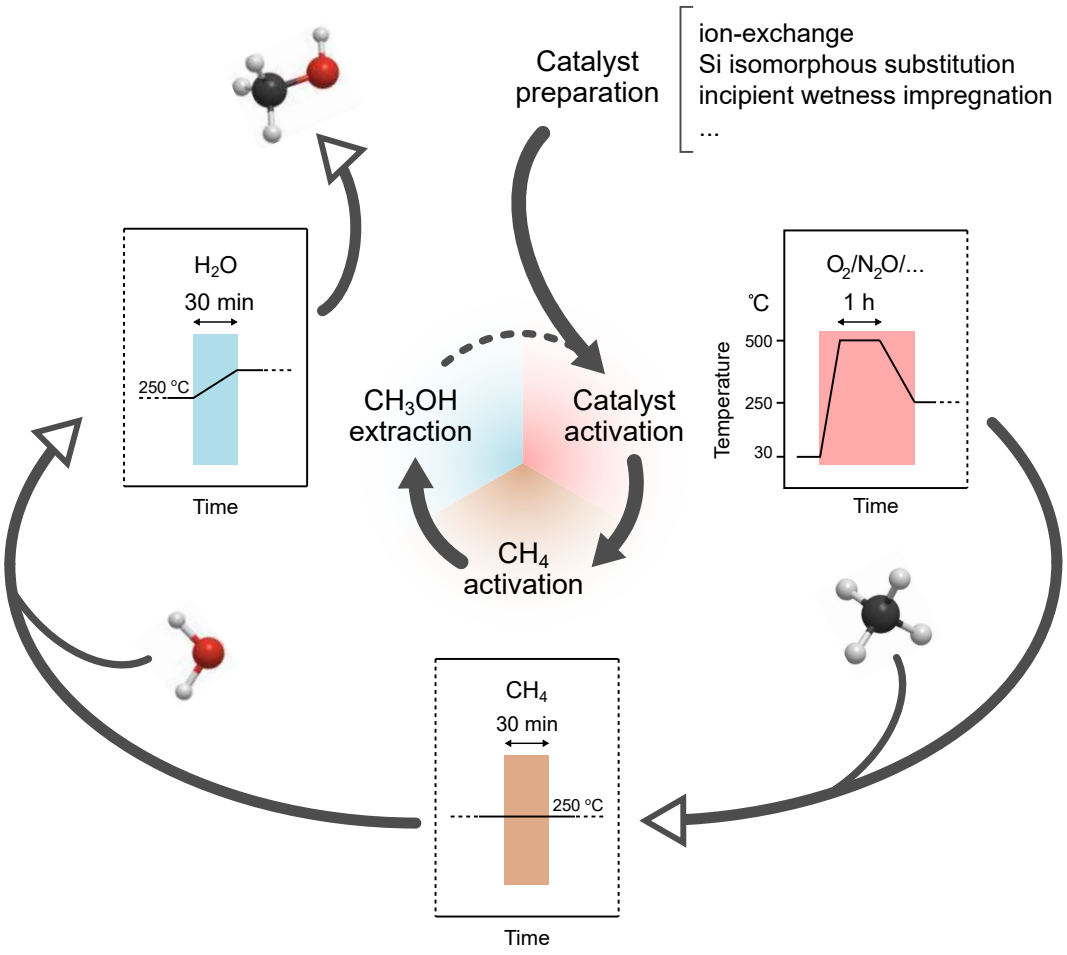

Figure 2.7: Schematic representation of a standard procedure for the direct conversion of methane to methanol.

Our idea

Assuming that CH_4 activation and CH_3OH extraction are the two key steps in the DCMM, it is clear that the ability of the zeolite to desorb methanol after dissociatevely adsorbing and partially oxidizing methane is of major importance. A parameter that can influence such ability is the acidity of the zeolite. As discussed in Section 2.1, only by adding a metal other than Al in framework position *prior* to crystallization one can tune the acidity strength of the BASs. In this perspective, we want to investigate whether the lower acidity of zeotypes containing *ad hoc* metals compared to the parent zeolites facilitates the desorption of methanol due to the lower adsorption strength of the zeotype towards methanol, or its precursor.

Take-home message

The direct conversion of methane to methanol is desirable from energy, economy and sustainability perspectives, and zeotypes are among the most promising catalysts for this reaction. However, most of the methanol precursors tend to remain adsorbed on the zeolite surface after methane is activated by the active sites present in the zeotype structure. The lower acidity of zeotypes compared to their parent zeolites promotes methanol desorption, and therefore is a key descriptor of the direct conversion of methane to methanol.

Methodology 3

3.1 Synthesis of the zeotype samples

Preparation of the samples in the H^+-form

Silicalite samples were prepared with sol-gel synthesis method followed by hydrothermal crystallization by incorporating Al (Al-S), B (B-S), Fe (Fe-S), Ga (Ga-S) and Ti (Ti-S) in the MFI framework. [1] The chemicals used for the synthesis are shown in Table 3.1.

1: Additionally, a pure silicalite sample (S) and a sample containing both Fe and Al (Fe/Al-S) were prepared.

Table 3.1: Chemicals used for the synthesis.
a Tetraethyl orthosilicate, reagent grade, 98%, Sigma Aldrich;
b Tetrapropylammonium hydroxide, 1.0 M Lsg. in water, Sigma-Aldrich;
c Technical, anhydrous, Sigma Aldrich;
d Fluka Chemicals;
e 98+% metal basis, Alfa Aesar;
f Ga 9-10 wt.%, Alfa Aesar;
g Aldrich.

Name	Formula	Use
TEOS [a]	$Si(OC_2H_5)_4$	silica source
TPAOH [b]	$C_{12}H_{29}NO$	SDA
Sodium aluminate [c]	$NaAlO_3$	Al precursor
Boric acid [d]	H_3BO_3	B precursor
Iron nitrate [e]	$Fe(NO_3)_3 \cdot 9\,H_2O$	Fe precursor
Gallium nitrate [f]	$Ga(NO_3)_3$	Ga precursor
Titanium ethoxide [g]	$Ti_4(OCH_2CH_3)_{16}$	Ti precursor

Oxalic acid (98%, Sigma-Aldrich) and sodium hydroxide (pellets, 98%, Alfa Aesar) were used to adjust the pH value. The calculated molar ratio Si:Me:TPA^+:H_2O = 1:0.02:0.300:24.86 was kept constant in all syntheses (Me = Al, B, Fe, Ga or Ti). [2] The basic idea was to use the same molar amount of substituting metal for each sample in order to be able to better compare the resulting materials properties.

2: In Fe/Al-S, the ratios Si/Al = Si/Fe = 100 were used.

In a standard synthesis procedure, the silica precursor was mixed with the structure directing agent, SDA, and the metal precursor in aqueous medium. The so obtained gel was crystallized in autoclave and the product was washed, filtered and dried. The SDA was then removed by calcination and the NH_4^+-form of the zeotypes was obtained by NH_4^+-exchange. The active H^+-form of the zeotypes was obtained by further calcination in air of the NH_4^+-form of the zeotypes. The NH_4^+-exchange and the latter calcination were not performed for the pure silicalite sample. [3]

3: See Papers I and IV for more detailed synthesis procedures.

Addition of Fe to the zeotype samples

Fe was added to 0.5 g of calcined silicalite sample by incipient wetness impregnation. The Fe source and the Si/Fe ratio used for

the impregnation were the same of the ones used for the synthesis of Fe-S. The so obtained wet sample powder was freeze-dried over night to remove the solvent and calcined for 2 hours at 500 °C, starting from room temperature with a heating rate of 5 °C min^{-1}.

Fe was also added by aqueous ion-exchange to all samples in the H^+-form. The Fe source was the same of the one used for the synthesis of Fe-S and the ratio Si/Fe = 3 was used. In particular, 1 g of sample was mixed with 100 ml of water and the Fe source for 24 h at room temperature. The so obtained wet powder sample was washed, filtered and freeze-dried over night to remove the solvent.

Take-home message

Pure silicalite and Al-, B-, Fe-, Fe/Al, Ga- and Ti-silicalite samples with the MFI framework were synthesized with sol-gel method and hydrothermal crystallization. The pure silicalite sample was further impregnated with Fe and all samples in the H^+-form were ion-exchanged with Fe.

3.2 Characterization of the zeotype samples

Electron microscopy

Electron microscopy is based on the interaction of electrons with matter. In the scanning mode, the primary electron beam hits the sample and the scattered electrons are detected. In particular the secondary electrons and the backscattered electrons give information about the morphology and the chemical composition of the sample, respectively. In the transmission mode, the electrons which are transmitted through the sample are collected by the detector to form the image.

In this work, scanning and transmission electron microscopy, SEM and TEM, were used to characterize the morphology of the synthesized zeotype crystals. The SEM images of the crystallites were taken with a Zeiss Ultra 55 FEG scanning electron microscope. The TEM images of the crystallites were taken with a FEI Tecnai T20 transmission electron microscope.

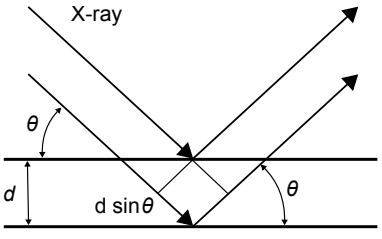

Figure 3.1: Schematic representation of the Bragg's relation.

X-ray diffraction

X-ray diffraction is based on the elastic scattering of X-ray photons by atoms in a crystal lattice. When the X-rays hit the sample, the

scattered monochromatic X-rays that are in phase give constructive interference. The lattice spacings between the crystal planes is derived using the Bragg relation, illustrated in Figure 3.1: $n\lambda = 2d \sin\theta$. [4] X-ray diffraction is a technique used to identify crystalline phases as well as to obtain information about particle size.

4: where n is an integer called order of reflection, λ is the wavelength of the X-rays, d is the distance between the crystal planes and θ is the angle between the normal to the reflecting crystal plane and the incoming X-rays. Because n, λ and θ are known values, d can be calculated and thus the crystal lattice parameters identified.

In this work, powder X-ray diffraction was used to confirm the MFI type of framework structure of the as synthesized samples and to confirm the hydrothermal stability of the calcined silicalite sample and of the metal-containing zeotype samples in the H^+-form after calcination. The X-ray diffractograms were taken with a Bruker XRD D8 advanced instrument with monochromatic CuKα radiation scanning from 5 to 55°.

Nitrogen sorption

In nitrogen physisorption experiments, N_2 molecules are physisorbed on the internal surface of a porous material and the amount of molecules needed to form a complete monolayer is calculated. [5] The measurement is performed isothermally and the volume of adsorbed (desorbed) nitrogen increasing (decreasing) the pressure is measured. The shape of the isotherms in the plot of adsorbed N_2 volume *versus* relative pressure gives information about the porous structure of the analyzed sample. [6]

5: In ideal conditions, this monolayer forms simultaneously in all pores. Nevertheless, capillary pore condensation depending on the pore sizes and multilayer grow may occur in real porous materials.

6: For example, microporous materials like zeolites show an hysteresis loop generated by the adsorption and desorption isotherms after the formation of the monolayer, due to the capillary condensation effects of the adsorbate molecules at high pressures.

The Brunauer-Emmett-Teller (BET) theory [49] is used to obtain information about the surface area and the pore volume of a porous material. This theory is based on several assumptions and for this reason is not strictly valid for microporous materials like zeolites. Nevertheless, it can be used as comparative method between different zeolite and zeotype samples.

In this work, N_2 physisorption was used to compare the specific surface area and the micropore volume of the silicalite samples. Moreover, the adsorption isotherms gave further information about the microporous structure and the metal incorporation in the framework. The nitrogen isotherms were measured by a Micrometrics Tristar 3000 instrument at -196 °C after degassing in N_2 at 220 °C for 5 h.

Polarized Raman spectroscopy

When infrared radiation interacts with matter, it can be transmitted, reflected, scattered or absorbed (see Figure 3.2). Raman spectroscopy is based on the inelastic scattering of infrared light, and most spectrometers are equipped with detectors capable of collecting the Stokes-scattered light. [7] The incident light induces a

7: The scattered light can have lower, higher or the same energy of the incident light (namely Stokes, anti-Stokes and Rayleigh scattering phenomena).

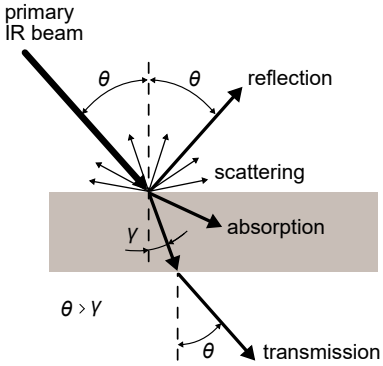

Figure 3.2: Schematic representations of the interaction of infrared light with matter.

dipole moment in the molecule or group of molecules investigated and therefore, the scattered light is characteristic for each type of chemical species and bonds.

The induced dipole moment ($\overrightarrow{\mu}$) in a certain chemical species is proportional to the induced electric field ($\overrightarrow{E}$) as: $\overrightarrow{\mu} = \alpha \overrightarrow{E}$, where α is called polarizability. In standard Raman spectroscopy, α is considered as a scalar as no distinction is made among the polarization directions of the incident light, which therefore is said circularly polarized. In polarized Raman spectroscopy, instead, the incident light is polarized and therefore the polarizability becomes a tensor ($\mathbf{A}^{3,3}$). Therefore, anisotropic vibrations will result in emphasized peaks in the Raman spectrum depending on the polarization of the incident light. In this way, information about the local structure of a sample can be derived. Furthermore, by placing an analyser between the sample and the detector, the scattered light can be polarized as well, and therefore information about the direction of the anisotropy can be deduced.

In this work, polarized Raman spectroscopy was used to further characterize the microstructure of the zeotype samples. Particular attention was given to the anisotropy of pure silicalite and to the influence of the incorporation of Al in the MFI framework on the local microstructure. [8] A more detailed description of the technique and the experimental set-up is reported in Paper II. The Raman spectra were recorded with an InVia Reflex spectrometer from Renishaw.

8: Raman spectroscopy experiments were performed for Fe-S and Fe/Al-S as well. For these samples, the high-frequency laser had to be used to avoid fluorescence phenomena. However, polarized experiments could not be performed since only the low-frequency laser was equipped accordingly.

Diffuse reflectance infrared Fourier transform spectroscopy

As mentioned above, the IR radiation can be transmitted, reflected, scattered or absorbed when it interacts with matter. When the IR beam is absorbed, it makes the bonds of the atoms and the molecules composing the material to vibrate. In the classical model, the chemical bonds between two atoms can be represented by two masses whose centers are kept together by a weightless elastic spring. [9] Because electrons are not considered in the classical model, a more accurate model is needed to describe the interaction of the IR radiation with matter. In the quantum model, the electronic configuration of an atom is represented as a landscape of discrete energy levels. In this perspective, the IR photons may cause energy transitions, whose intensity corresponds to the IR frequency between the vibrational levels of a chemical bond. Each chemical bond is characterized by specific energy transitions of the vibrational levels, which in turn are sensitive to the surrounding environment.

9: The law which regulates the vibrations in the classical model is the Hooke's law, where the force of the chemical bond depends on the elastic force constant and the masses representing the atoms.

In IR spectroscopy, the phenomenon of IR absorption of matter is exploited to obtain information about the chemical composition of the sample. The IR beam hits the sample and makes the chemical bonds of the sample to vibrate at specific frequencies as described above. Thus, the IR spectrum of a substance can be considered as the "fingerprint" of the substance where each peak represents the vibrational modes of a unique species. [10]

The most common mode of operation for IR spectroscopy is transmission, where the IR beam is transmitted through the sample. [11] Although in transmission IR spectroscopy quantitative measurements are more accessible, it is difficult to study the evolution of the surface species when adsorbing probe molecules on the sample. When, instead, IR spectroscopy operates in diffuse reflectance mode the evolution of adsorbed surface species can be followed *in situ*. The incident IR radiation is scattered by each particle in the combined process of diffraction, refraction and reflection. The fraction of the radiation which reemerges from the surface is said to be diffusely reflected. [12]

In this work, all IR spectra were recorded by an FTIR spectrometer in diffuse reflectance mode (diffuse reflectance infrared Fourier transform spectroscopy, DRIFTS). In particular, the spectra were recorded using a VERTEX 70 spectrometer (Bruker) equipped with a liquid nitrogen cooled mercury cadmium telluride (MCT) detector (bandwidth 600-12000 cm^{-1}), a Praying Mantis™ accessory and a high-temperature stainless steel reaction chamber (Harrick Scientific Products, Inc.). The setup of DRIFTS used in this work is schematically illustrated in Figure 3.3b. The IR beam is generated by an IR source and goes through a Michelson interferometer. A Praying Mantis™ element consisting of several mirrors focus the IR beam on the sample surface, which diffusely reflects the radiation. The reflected radiation is then directed to the detector

10: Probe molecules (*e.g.* NH_3, NO, CO, *etc.*) can be adsorbed on the sample and their interaction with the sample surface can give further information about the functional groups. Commonly, a background spectrum is recorded as reference and is subtracted to the following spectra to better visualize the evolution of the chemical species.

11: A typical IR spectrum has wavenumbers [cm^{-1}] ($\propto 1/\text{frequency}$, ν) in the x axis, whilst the quantity reported in the y axis depends on the mode of operation of the instrument. When in transmission mode, the transmittance, $T(\nu)$ (*i.e.* the ratio of the intensity of the light transmitted through the sample and the intensity of the source radiation) or the absorbance, $A(\nu)$ ($A(\nu) = \log_{10}(1/T(\nu))$) is plotted as a function of the wavenumbers in a standard spectrum.

12: Similarly to the transmittance, the reflectance, $R(\nu)$, is given as the ratio between the intensity of the light diffusely reflected by the sample and the intensity of a non-absorbing reference, *i.e.* KBr, and is plotted as a function of the wavenumbers.

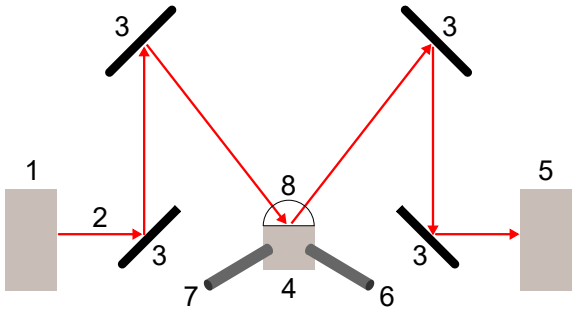

1: IR source
2: IR beam
3: mirrors
4: sample
5: detector
6: gas inlet
7: gas outlet
8: dhome

Figure 3.3: Schematic representations of the DRIFTS setup used in this work.

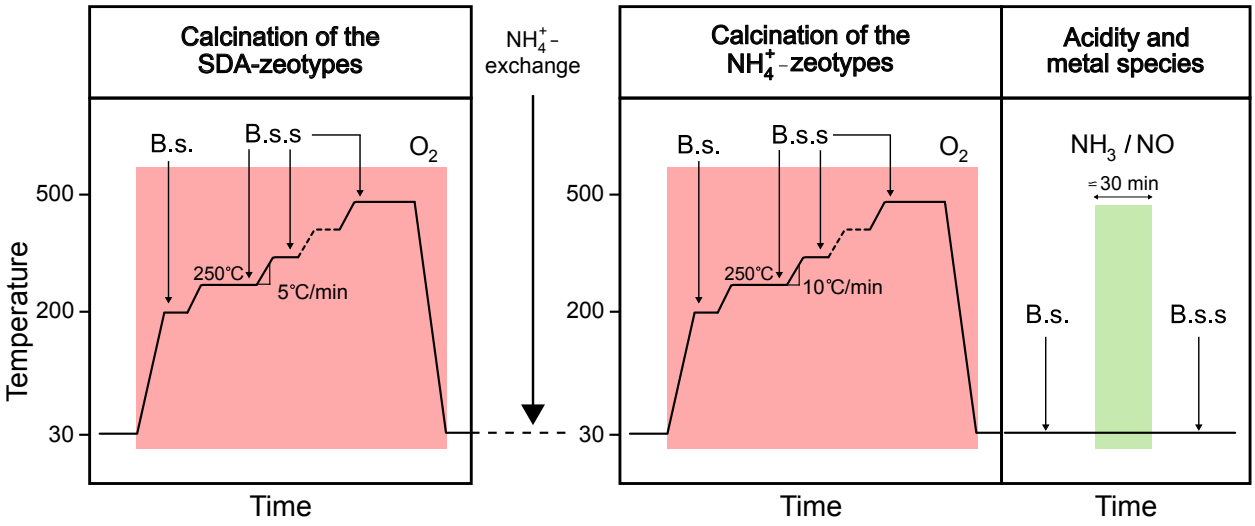

Figure 3.4: Schematic representation of the experiments performed by DRIFTS (B.s. = background spectrum, B.s.s.= background subtracted spectra).

by mirrors and Fourier transformed to the final spectrum. A high-temperature stainless steel reaction chamber (Harrick Scientific Products, Inc.) is used to control the sample temperature and the gas flow throw the sample. A schematic representation of all IR experiments performed in this work is shown in Figure 3.4. [13]

13: The entire process from the removal of the SDA from the framework to the activation of the zeotype into the acid H^+-form was examined by DRIFTS. Furthermore, experiments with NH_3 and NO as probe molecules were also performed and the adsorbed surface species were investigated with DRIFTS.

Take-home message

The zeotype crystallites were imaged with SEM and TEM and their microstructure characterized with XRD, N_2-sorption and polarized Raman spectroscopy. The elimination of the SDA from the microsctructure and the activation of the zeotype from the NH_4^+- to the H^+-form were followed *in situ* with DRIFTS. Particular attention was given to the O−H stretching region of the spectra of the samples in the H^+-form to investigate the Brønsted acidity.

3.3 Temperature programmed desorption of methanol with DRIFTS

DRIFTS was used to monitor the evolution of the surface species during methanol temperature programmed desorption (CH_3OH-TPD). Albeit aware that CH_3OH-TPD does not fully reproduce the last step in the DCMM reaction cycle, this experiment is performed to simulate the extraction of CH_3OH in the DCMM. In particular, each sample [14] was exposed to methanol and the evolution of the formed surface species was followed with DRIFTS while increasing

14: The CH_3OH-TPD experiments were performed for all samples in the H^+-form, S and all Fe-exchanged samples.

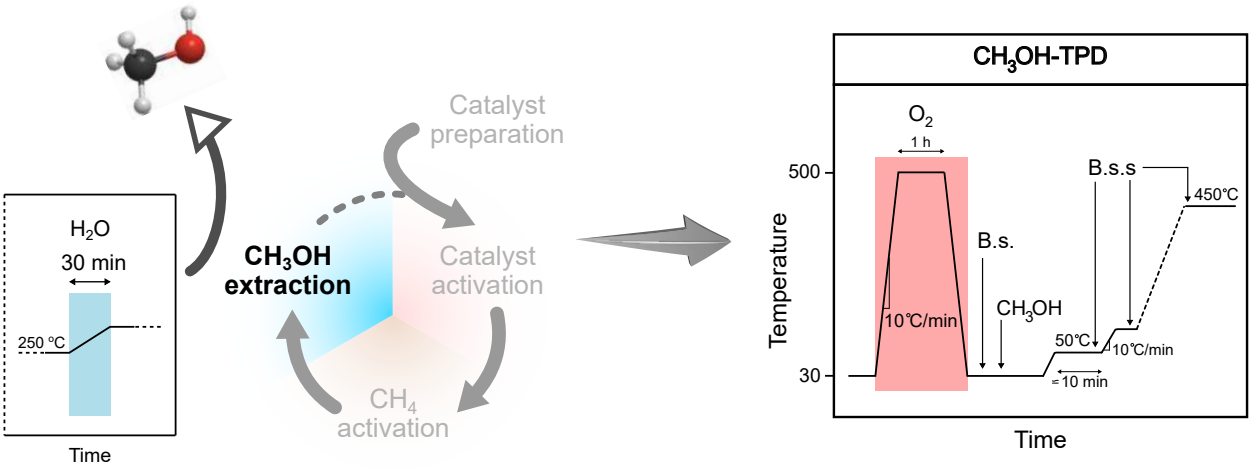

Figure 3.5: Schematic representations of the CH_3OH-TPD experiments with DRIFTS used to simulate CH_3OH extraction in the DCMM (B.s. = background spectrum, B.s.s.= background subtracted spectra).

temperature from 30 to 450 °C. A schematic representation of the experiments is shown in Figure 3.5.

Take-home message

The evolution of the surface species during temperature programmed desorption of methanol was followed *in situ* with DRIFTS for all samples in the H^+-form and for all Fe-exchanged samples.

3.4 Methane exposure with DRIFTS

In order to investigate whether the zeotype samples are capable of activating CH_4 or not, S, Al-S, Fe-S and Fe/Al-S were exposed to CH_4 at 250 °C and the surface species were examined with DRIFTS. [15] As for the previous experiments, albeit aware that CH_4 exposure does not fully reproduce the first step in the DCMM reaction cycle, this experiment is performed to simulate the activation of CH_4 in the DCMM.

A schematic representation of the experiments is illustrated in Figure 3.6. The pretreatments in O_2 and N_2O were performed to clean the surface of the samples from possible impurities and to form the reactive sites in the Fe-containing samples, respectively. After CH_4 exposure, all samples were exposed to water to examine the tendency of the zeotypes internal surfaces to desorb the reaction products.

15: These experiments were performed only on the aforementioned samples since they belong to the first synthesis batch. Further investigation on B-S, Ga-S and Ti-S, and the Fe-exchanged samples would give a more detailed overall view on the CH_4 exposure experiments.

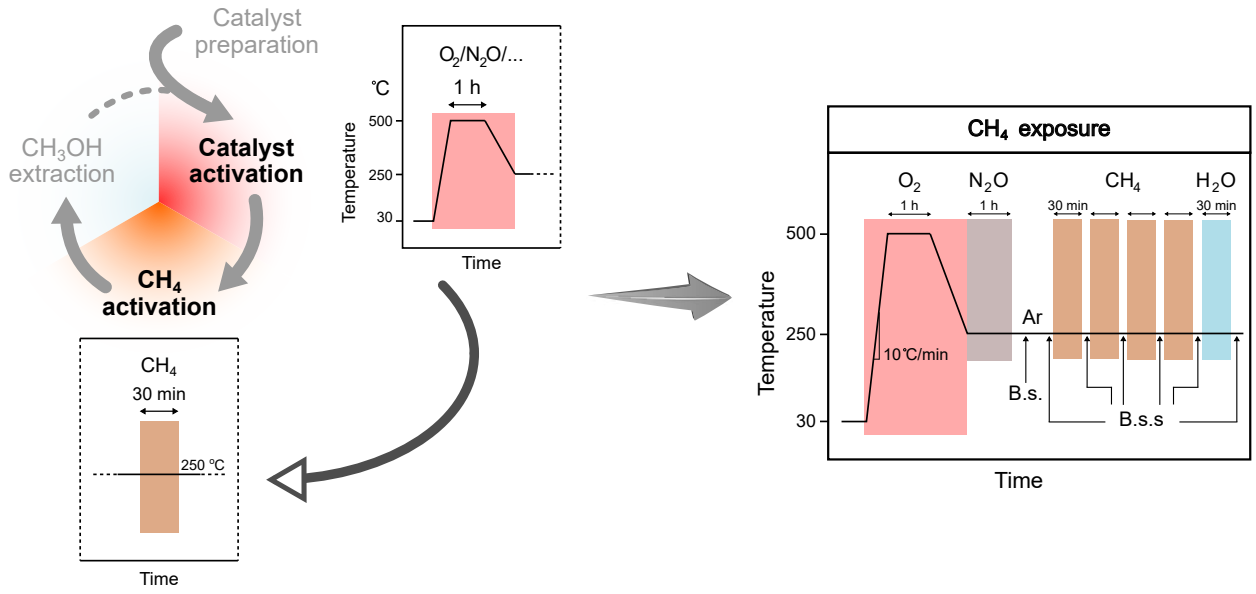

Figure 3.6: Schematic representations of the CH_4 exposure experiments with DRIFTS used to simulate CH_4 activation in the DCMM (B.s. = background spectrum, B.s.s.= background subtracted spectra).

Take-home message

The formation and evolution of methoxy *ad*-species were investigated with DRIFTS while exposing the samples in the H^+ form to methane and to water.

3.5 Bird's-eye view on the experiments performed on the zeotype samples

In Figure 3.7 a summary of all experiments performed in this study is reported, together with the relative Sections in this thesis.

Sample		Microscopy		XRD	N_2 sorption	Polarized Raman Spectroscopy	DRIFTS				CH_3OH-TPD	CH_4 exposure
Code	Form	SEM	TEM				SDA to NH_4^+	NH_4^+ to H^+	H^+	NH_3 adsorption	NO adsorption	
S	SDA	4.1		4.1			4.2					
	calc.	4.1	4.1	4.1	4.1	4.1			4.2	4.2	4.2	5.2	5.2
	Fe-imp.								4.2			5.2	
Al-S	SDA	4.1		4.1	4.1		4.2						
	NH_4^+							4.2					
	H^+	4.1		4.1	4.1	4.1			4.2		4.2	5.2	5.2
	Fe_{ex}								4.2			5.2	
B-S	SDA	4.1		4.1	4.1		4.2						
	NH_4^+							4.2					
	H^+	4.1		4.1	4.1				4.2			5.2	
	Fe_{ex}								4.2			5.2	
Fe-S	SDA	4.1		4.1	4.1		4.2						
	NH_4^+							4.2					
	H^+	4.1		4.1	4.1				4.2	4.2	4.2	5.2	5.2
	Fe_{ex}								4.2			5.2	
Fe-Al/S	SDA	4.1		4.1	4.1		4.2						
	NH_4^+							4.2					
	H^+	4.1		4.1	4.1				4.2	4.2	4.2	5.2	5.2
	Fe_{ex}								4.2			5.2	
Ga-S	SDA	4.1		4.1	4.1		4.2						
	NH_4^+							4.2					
	H^+	4.1		4.1	4.1				4.2			5.2	
	Fe_{ex}								4.2			5.2	
Ti-S	SDA	4.1		4.1	4.1		4.2						
	NH_4^+							4.2					
	H^+	4.1		4.1	4.1				4.2			5.2	
	Fe_{ex}								4.2			5.2	

Figure 3.7: Summary of the samples investigated and the techniques used to characterize them, with reference to the relative Section in this thesis.

Materials characterization 4

4.1 Structural and morphological characterization

Images of the zeotype crystallites

The SEM images show high crystallinity of the zeotype samples (see Figure 4.1 and 4.2). [1] However, some differences can be observed depending on the metal added during synthesis regarding both the crystal morphology and the presence of impurities on the external facets of the crystals formed after calcination.

1: Remarkable is that we could observe with TEM the 10 MRs of the straight channels of the MFI framework of S, as shown on the top left of Figure 4.1.

Regarding the morphology, S, B-S and Al-S show individual crystals with homogeneous geometry, and a uniform particle size distribution with dimensions ranging between 10 and 25 μm. [2]. Further, the crystals of these samples show predominantly the typical MFI crystal shape of two elongated parallelepipeds embedded one in each other [50]. The Fe-containing samples (Fe-S and Fe/Al-S) additionally show crystals with a spherical shape, whilst Ga-S shows interconnected crystals with irregular shapes and a wider particle size distribution. Lastly, Ti-S shows overall more brittle crystals, with features of both B-S and Ga-S. These differences in the crystals morphology might be caused by the different metal precursors used during synthesis, but further investigations should be done to determine a solid correlation.

2: The crystals of S and Al-S (15 and 25 μm) are in average larger than the crystals of B-S (10 and 20 μm)

Regarding the impurities on the external facets of the crystals, all samples show formation of additional features after calcination, but in different amounts. S and Al-S show minor additional features than the crystalline material, whilst B-S, Fe-S, Fe/Al-S, Ga-S and Ti-S show that irregular structures are formed on the external facets of the zeotypes crystals during calcination. These structures might be due to the migration of the metals from the T-sites due to instability in the MFI framework. However, since we can conclude from the DRIFTS experiments that metal is still in the MFI framework of the samples in the H^+-form, these structures might also consist of SDA or other synthesis residues which were not completely eliminated during calcination. [3] Whatever the nature of these structures, it is noteworthy that the overall morphology of the crystals is maintained after calcination, indicating the thermal stability of the MFI framework.

3: The Fe-containing samples are more controversial though, since as discussed later in this Section and as it will be further considered in Section 4.2, some Fe used in the synthesis gel was not successfully incorporated in the framework in place of Si, but formed instead oxide and hydroxide clusters. Therefore, these additional features might also consist of extra framework Fe species which have not been incorporated in the zeotype framework during synthesis.

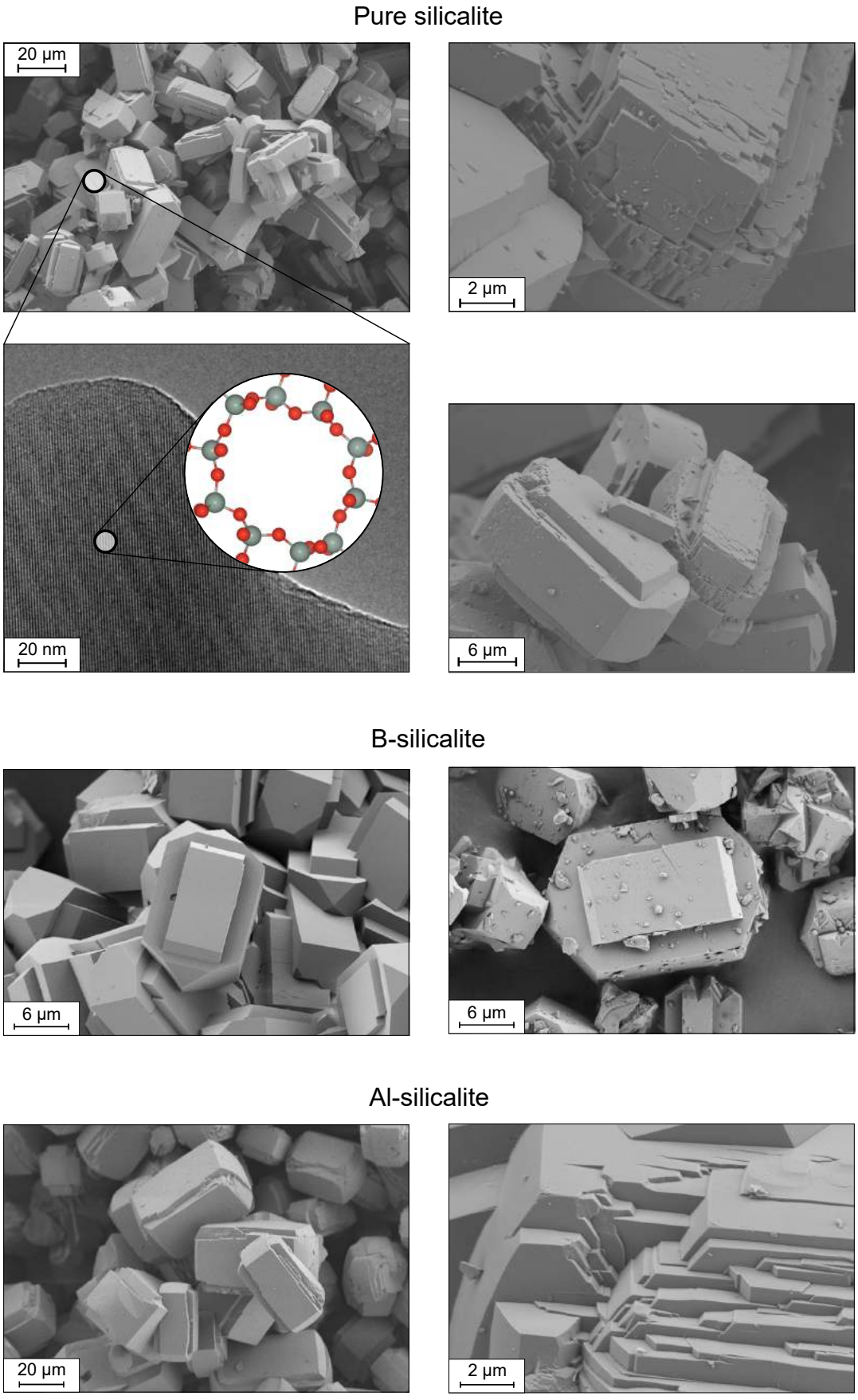

Figure 4.1: SEM images of the zeotype crystallites in the as synthesized form (left column) and H^+-form (right column), and TEM image of the 10 MR of a portion of pure silicalite crystallite, together with schematic representation of the 10 MR.

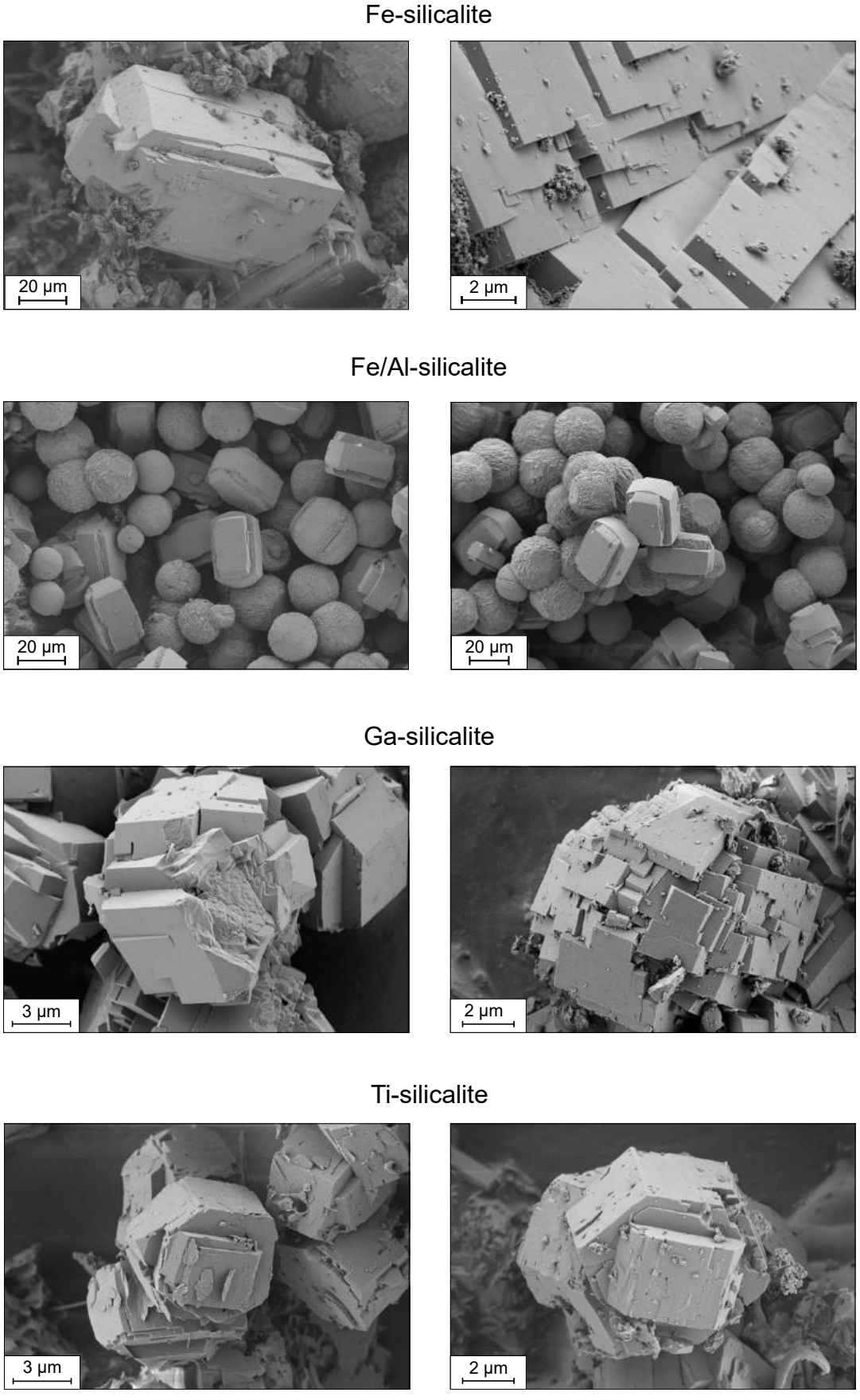

Figure 4.2: Continuation of Figure 4.1.

Analysis of the MFI framework and the microporous structure

The MFI type of framework structure of all samples is confirmed by XRD [21]. [4] The X-ray diffractograms of S before and after calcination are shown in Figure 4.4, together with the Miller indices of the crystal planes associated to the diffraction peaks with the highest intensities (indices taken from the Database of Zeolite Structure [51]). The X-ray diffractograms associated to the metal containing samples are shown in Figure A1. The thermal stability of the zeotype structure is confirmed by the absence of any peak shifts in the diffractograms of the samples after calcination compared to the diffractograms of the as synthesized samples. The changes of the intensities of some peaks as well as the disappearance of peaks at low 2θ values in the diffractogram of the calcined sample are due to the elimination of the SDA by calcination [51]. Extra peaks were expected in the diffractograms of the metal-containing samples if additional crystal phases to the MFI framework formed in sufficient amount to be detected by XRD. Also, peak shifts were expected if metals were incorporated in the MFI framework in sufficient amount to be detected by XRD. The absence of peak shifts and additional peaks suggests that the amount of metals incorporated in the MFI framework and the amount of any additional crystalline phases other than MFI are too low to be detected by XRD.

4: Several synthesis attempts were made before the one described in Section 3.1 and indeed, that is the result of an optimized synthesis procedure in terms of various parameters. Many samples synthesized after ineffective hydrothermal crystallization showed either amorphous phases either the typical MFI diffractogram but with a large bump distributed over a wide range of 2θ values. As example, the X-ray diffractogram of the as synthesized material after ineffective hydrothermal crystallization is shown in Figure 4.3.

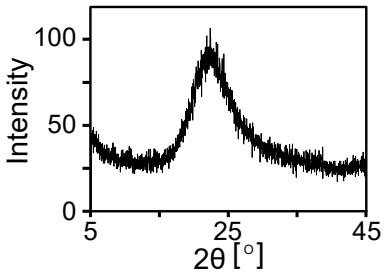

Figure 4.3: X-ray diffractogram of the as synthesized material after ineffective hydrothermal crystallization

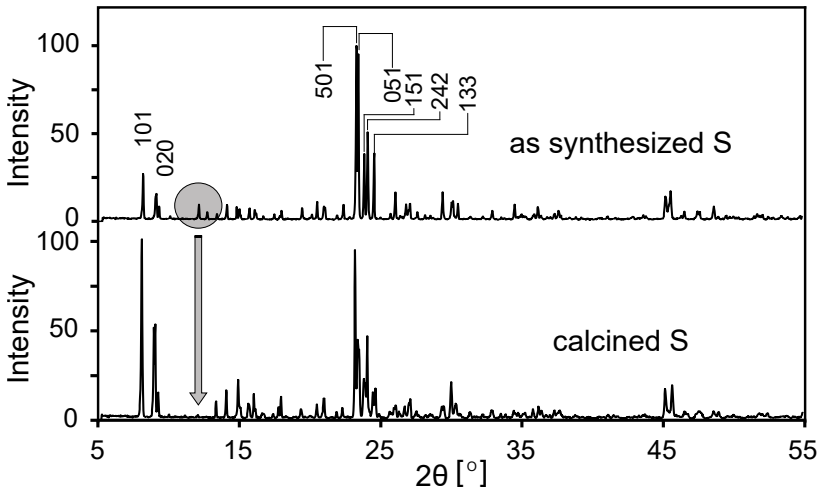

Figure 4.4: X-ray diffractograms of S before and after calcination, together with the Miller indices of the crystal planes associated to the diffraction peaks with the highest intensities. The disappearance of the peaks associated to the SDA after calcination is shown by the grey circle and arrow.

The results obtained by the nitrogen physisorption experiments (see Figure 4.5) show that all values are reasonable for the MFI type of framework structure [52]. It can be observed from Figure 4.5 and Table 4.1 that the values of BET surface area decrease with increasing crystal ionic radius of the metal incorporated in the MFI framework [53] (with Ti^{4+} being an outlier in the list). Therefore that the zeotype samples show different values of BET surface area might be due to the size of the element in framework position.

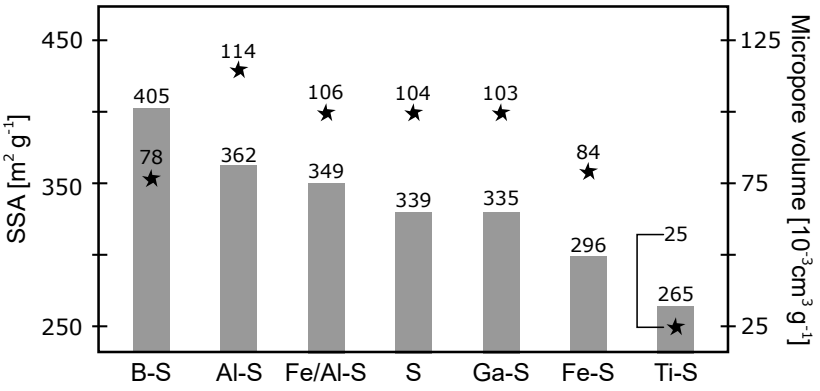

Figure 4.5: Specific BET surface area (SSA) and micropore volume of the samples in the H^+-form.

Regarding the micropore volume, the samples can be grouped in three categories:

- High micropore volume: S, Al-S, Fe/Al-S, S and Ga-S;
- Intermediate micropore volume: B-S and Fe-S;
- Low micropore volume: Ti-S.

However, no correlation with the crystal ionic radius can be outlined in this case. Nevertheless, the variation of the values of micropore volume is minor among the zeotype samples, being again Ti-S an outlier in this case as well. [5]

The N_2 sorption isotherms of all samples (see Figure 4.6) are of Type IV of the IUPAC classification [54] and therefore further confirm the microporous structure of the zeotype samples. However, different types of hysteresis can be observed according to the metal incorporated in the MFI framework: [6]

- Type H1 of hysteresis: S, Al-S, B-S, Fe-S, and Fe/Al-S;
- Type H4 of hysteresis: Ga-S;
- Combination of Type H1 and H4: Ti-S.

Type H1 of hysteresis indicates the presence of well-defined channels with uniform sizes and shapes [54, 55]. Since the majority of the zeotypes show this type of hysteresis, including the pure silicalite sample, it is reasonable to assume that S, Al-S, B-S, Fe-S, and Fe/Al-S present a more similar microporous structure to the pure MFI framework. Type H4 of hysteresis, instead, indicates materials containing both micropores and mesopores and is often found in zeolitic materials with aggregated crystals [54, 56]. Therefore, the microporous structure of Ga-S seems to present a less uniform geometry. The interpretations from the nitrogen sorption isotherms are indeed supported by the SEM images (Figures 4.1 and 4.2), where it was observed that S, Al-S, B-S, Fe-S, and Fe/Al-S are characterized by independent single crystals, whilst Ga-S shows agglomerates of crystals that might cause the formation of mesopores. [7] In this perspective, the isotherms of Ti-S suggest the presence of both a

Table 4.1: Crystal ionic radii (r_i) of the elements incorporated in the MFI framework.

Ion	r_i [pm]
B^{3+}	41
Al^{3+}	67
Ga^{3+}	76
Fe^{3+} †	78
Ti^{4+}	74

† Assuming low spin state of Fe^{3+}.

5: That Ti-S shows much lower values of BET surface area and micropore volume might be due to the presence of Ti species in extra-framework position, that either have not been successfully incorporated in the framework during synthesis, or migrated from the framework during calcination. However, further investigation should be done in this matter.

6: For clarity, the isotherms for one sample per category are shown in Figure 4.6.

7: As mentioned in Section 4.1 the Fe-containing samples actually show both parallelepiped and spherical shapes. However, the crystals do not show agglomerates and therefore the microporous structure with well-defined channels is likely maintained.

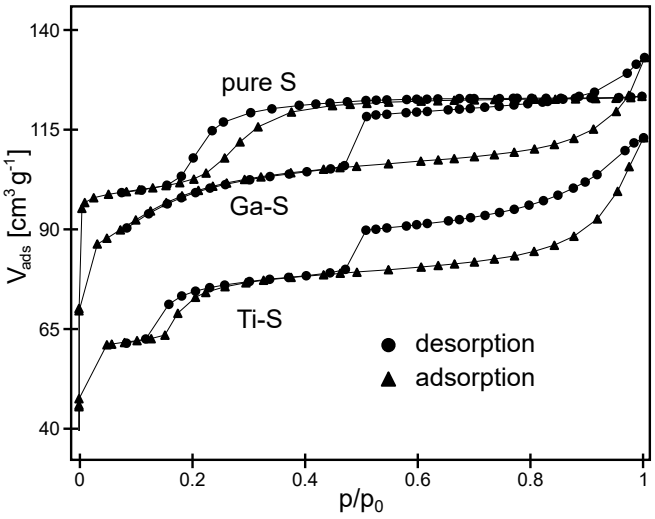

Figure 4.6: Nitrogen adsorption-desorption isotherms for the calcined pure, Ga- and Ti-silicalite samples.

well-defined porous structure, and mesopores. Indeed, the SEM images of Ti-S show both well-separated crystals and agglomerates of crystals.

More insights about the metal incorporation in the zeotype structure can be deducted by considering the N_2 adsorption isotherm of each sample (see Figure 4.7). [8] It has previously been found that the electrostatic interactions between the N_2 molecules and the internal surface of the zeolite can influence the shape of the adsorption isotherms [57]. For example, it has been found that ZSM-5 zeolites with high Si/Al ratios show at high relative pressures a second transition bump in the adsorption isotherm from liquid- to solid-like state of the adsorbate [58]. In particular, the increase of the amount of Al leads to a shift of this second transition towards higher relative pressures. In the present study, we observe a similar behavior, suggesting that different metals can influence the shape of the isotherms in a similar way as the Si/Al ratio does. In this

8: See Paper I for a more detailed explanation of this paragraph.

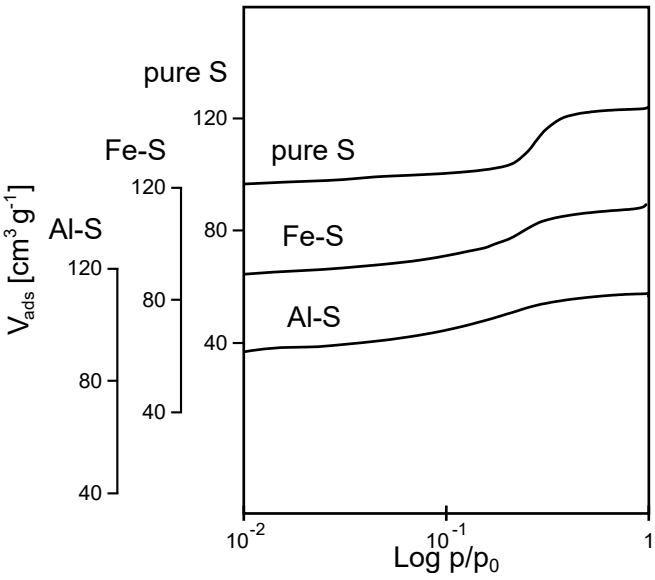

Figure 4.7: Nitrogen adsorption isotherms of the pure, Fe- and Al-silicalite samples.

perspective, three trends can be observed regarding the position and shape of the aforementioned second transition bump in the adsorption isotherm: [9]

- Pronounced bump at higher relative pressure: S, B-S and Ti-S;
- Modest bump at lower relative pressure: Al-S and Ga-S;
- Intermediate behavior: Fe-S and Fe/Al-S.

Therefore, it seems that the incorporation of some metals in the MFI framework leads to different adsorbate-adsorbent electrostatic interactions. The parallelisms that these interactions might have with the acidity of the samples will be further discussed.

9: For clarity, the isotherm of one sample per trend is shown in Figure 4.7.

Investigation of the local anisotropy of the zeotype crystals

Polarized Raman spectroscopy has been used in order to characterize the local anisotropy of the crystals of S and Al-S. [10] Indeed, since the MFI framework is not isotropic in the different crystal axes, bands related to elements that predominantly occur in one direction can be emphasized by polarizing the incident light. The Raman spectra of the pure silicalite sample recorded without analyzer at different polarization configurations are shown in Figure 4.8. It is well established in the literature that the Si−O−Si bending and the O−Si−O and Si−O−Si stretching regions are observed below and above 600 cm^{-1}, respectively [59–62]. Furthermore, the peaks in the region below 600 cm^{-1} are expected to red shift with increasing ring size, and their intensities to increase with the frequency [63]. However, a clear assignment of some vibrational modes, for example of the ones related to member rings of different size, is still under debate. [11]

10: The Polarized Raman spectroscopy experiments were not performed by me and therefore only the results that are most relevant for this thesis are reported here below. A more comprehensive interpretation of the results from the polarized Raman spectroscopy experiments can be found in Paper II.

11: Indeed, the vibrations of the 10, 6, 5 and 4 MR of the MFI framework are energetically close to each other, and depend on several factors, *e.g.* bond angle, ring size and type of sub-unit connection.

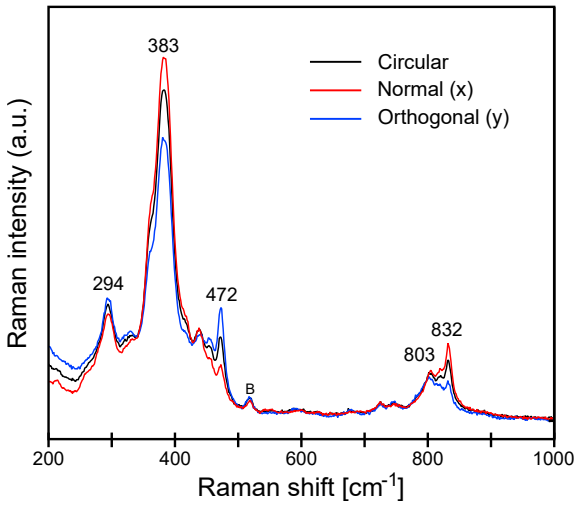

Figure 4.8: Raman spectra collected from the upper *a-c* plane of a single crystal of S with the incident light being circularly (black line), normally (blue line) and orthogonally (red line) polarized.

Based on these considerations and in line with previous studies, the peaks at 472, 383, 360 and 294 cm^{-1} of Figure 4.8 are assigned to the Si–O–Si bending vibrations of the 4, 5, 6 and 10 MR, and the peak at 832 cm^{-1} to the stretching of the Si–O–Si bonds shared between 5 MRs. [12] The novelty of Figure 4.8 consists on the dependence of the intensity of the aforementioned peaks on the polarization of the incident light. For example, the peak at 472 cm^{-1}, and the peaks at 383 and 832 cm^{-1} are emphasized when the incident light is normally and orthogonally polarized, respectively. [13] Moreover, as expected, the intensities of these peaks are intermediate when the incident light is circularly polarized. These aspects are therefore a direct manifestation of the anisotropy of the MFI framework structure and have not been shown before in the literature.

12: See Figure 2.3 for a detailed representation of the MFI framework.

13: The 4 MR are only present in the *a-c* plane of the silicalite crystal, and therefore, in the laboratory coordinates, are visible only when the incident light is normally polarized.

The Raman spectrum of Al-S shows that the characteristic frequencies and the relative intensities are the same of the ones of the Raman spectrum of S (Figure 4.9a), confirming the integrity of the MFI framework after the isomorphous substitution of Si with Al. However, the peaks of the spectrum of Al-S are overall broader, indicating an increased disorder in the MFI framework. The peak at 472 cm^{-1} is the least affected by this line broadening, suggesting that the 4 MRs are the least probable sites for the Al atoms. [14] Further information about the local anisotropy of Al-S could be obtained by considering different polarization of the incident light (see Figure 4.9b). [15] The peak at 3611 cm^{-1} is assigned to the O–H stretching vibration of the Brønsted acid sites generated by Al, and will be discussed in detail in the results of the DRIFTS experiments in Section 4.2. The peak at 3663 cm^{-1} is not observed in the DRIFTS experiments and is assigned to the O–H stretching of Al species in extra-framework position [64]. Both peaks are more emphasized when the incident light is polarized along the *a*-axes of the zeotype crystal, suggesting that the –OH groups are likely oriented towards this direction.

14: Another difference in the spectra of S and Al-S is the presence of a peak at 974 cm^{-1}, assigned to Al–OH stretching with the Al sitting at the positions shared between 5 MRs.

15: Here the O–H stretching region could be recorded thanks to a high frequency laser coupled with appropriate grating.

Take-home message

The SEM and TEM images showed high crystallinity of all prepared zeotype samples, and that the use of different metal precursors led to some differences in the crystals morphology. XRD confirmed that all samples show the MFI type of framework structure. The microporous structure was further confirmed by N_2 sorption, that gave additional information about metal incorporation. Polarized Raman spectroscopy allowed to clarify previous assignments found in the literature of some peaks related to the *n*-member rings of the MFI framework and to speculate on the position of the Brønsted acid sites in the Al-silicalite sample.

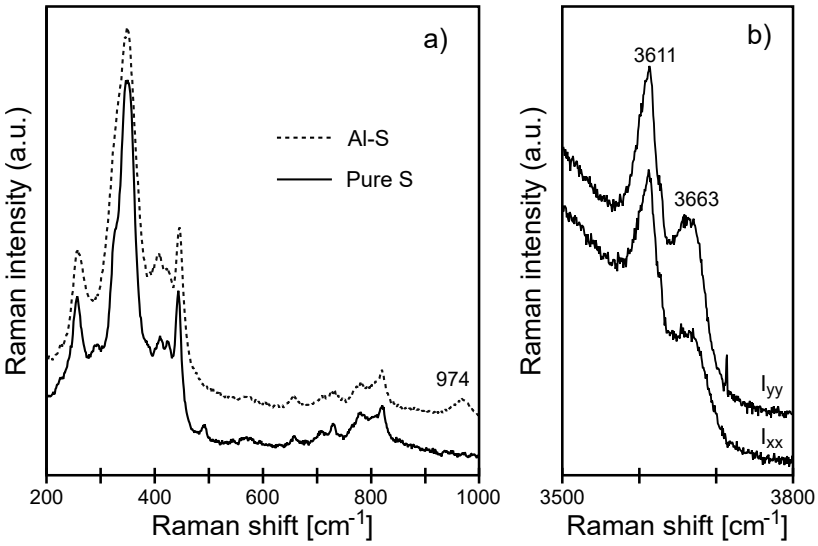

Figure 4.9: a) Raman spectra collected from single crystals of S and Al-S with the polarization of the incident light parallel to the c-axis. b) High frequeny range of Raman spectra recorded at parallel conditions with the polarization of the incident laser parallel to the c-axis (I_{xx}) or the a-axis (I_{yy}).

4.2 Chemical characterization of the samples using DRIFTS

From the SDA- to the H^+-form of the zeotype samples

The removal of the SDA from the zeotype channels by calcination was followed by DRIFTS for all samples. [16] As example, the spectral series of S is presented in Figure 4.10. The doublet of absorption peaks at 2330 and 2440 cm^{-1} which appears at around 350 °C clearly indicates the formation of CO_2 and thus the complete oxidation of the propyl chains of the TPA^+ ions. The negative absorption peaks at 2880, 2944 and 2980 cm^{-1} are assigned to C–H stretching vibrations of the propyl chains of the TPA^+ ions [65, 66] and thus indicate elimination of the SDA. [17] The positive absorption

16: See Paper I form a more detailed explanation of this paragraph.

17: The difference in temperature at which the doublet of peaks at 2330 and 2440 cm^{-1}, and the peaks at 2880, 2944 and 2980 cm^{-1} appear, might be related to the Van der Waals interactions between the SDA and the channels in the as synthesized zeotype discussed in Section 2.2. Indeed, by increasing the temperature in an oxidizing environment, the SDA likely first loses contact with the framework and only at higher temperatures it oxidizes, ultimately to CO_2.

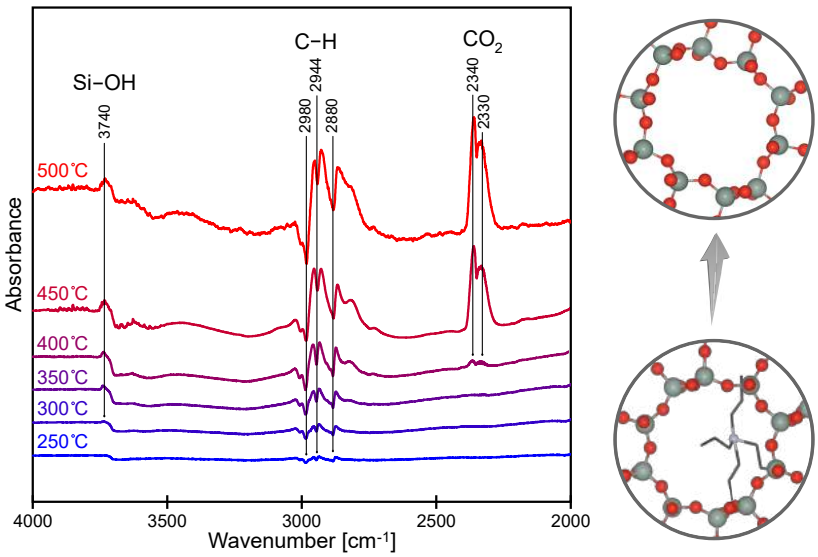

Figure 4.10: Background subtracted IR spectra of the as synthesized silicalite sample recorded during calcination in 10% O_2/Ar from 250 to 500 °C. The background spectrum was taken at 200 °C in 10% O_2/Ar.

peak at 3740 cm^{-1} is assigned to the O–H stretching vibrations of the terminal silanol groups (≡Si–OH) and is typical for silica based materials [67]. This peak forms and evolves concurrently with the absorption peaks in the C–H stretching vibrations region assigned to the elimination of the SDA. This fact suggests that the silanol groups become IR visible as soon as the TPA^+ ions lose contact with the internal surface of the zeotype and thus is in line with the fact that the TPA^+ ions interact via Van der Waals interactions with the surface of the zeotype.

The activation of the zeotypes from the NH_4^+- to the H^+-form by calcination was followed by DRIFTS for all samples. As example, the spectral series of Fe-S is presented in Figure 4.11. The negative absorption peaks at 2880 and 2944 cm^{-1} are again assigned to the C–H stretching vibrations of the propyl chains of the TPA^+ ions and thus indicate that not all SDA was removed during the calcination of the as synthesized sample. [18] The negative absorption peak at 3370 cm^{-1} is assigned to N–H stretching vibrations and thus indicates the activation of the zeotype from the NH_4^+- to the H^+-form. Absorption peaks other than the absorption peak assigned to terminal silanol groups appear in the O–H stretching vibration region. The facts that the position of these peaks depends on the metal added during synthesis and that they evolve together with the absorption peak at 3370 cm^{-1} suggest that these –OH groups belong to the zeotype Brønsted acid sites, BASs (≡Si–O(H)–Me≡, Me = Al, B, Fe, Ga). Ti-S shows only one sharp absorption peak in the O–H stretching vibration region at 3735 cm^{-1}, assigned to the O–H stretching of Si–OH. [19] Indeed Ti-S is not expected to present any Brønsted acidity, since the oxidation state of Ti is +4 and therefore the electroneutrality of the framework is maintained when Ti^{4+} substitutes Si^{4+} [68].

18: These absorption peaks are not present in the spectra of B-S, Ga-S and Ti-S (see Paper IV), suggesting that most of the SDA was removed during the calcination of the as synthesized sample. However it should be noted that in Figure 4.11 the intensities of these absorption peaks are very weak.

19: See Figure S3b in the Supplementary Information of Paper IV.

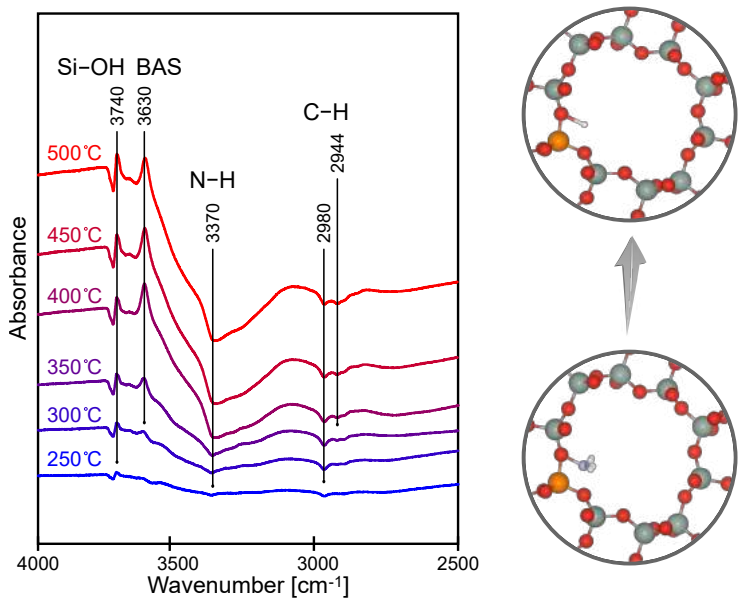

Figure 4.11: Background subtracted IR spectra of Fe-S in the NH_4^+-form recorded during calcination in 10% O_2/Ar from 250 to 500 °C.The background spectrum was taken at 200 °C in 10% O_2/Ar.

Acidity of the zeotype samples

In Figure 4.12 the spectra recorded at room temperature in Ar after calcination of all samples in the NH_4^+-form are presented. As previously mentioned, the position of the absorption peak assigned to the O−H stretching vibrations of the −OH groups belonging to the BASs depends on the metal incorporated in the MFI framework during synthesis. The position of the BASs peak is caused by the different influence the heteroatoms have on the −OH groups belonging to the BASs (see Section 2.1 for a more detailed explanation). Finally, the following series of increasing acidity can be outlined: [20]

$$0 = S = Ti\text{-}S < B\text{-}S < Fe\text{-}S < Fe/Al\text{-}S < Ga\text{-}S < Al\text{-}S$$

20: The fact that Fe/Al-S shows a broader and less intense peak centered at 3620 cm^{-1} is likely due to the presence of two types of BASs (one generated by Fe and one by Al) whose absorption peaks overlap in the IR spectrum. S and Ti-S show no peaks other than the peak assigned to the terminal silanol groups in this region. Indeed, as mentioned before, S and Ti-S are not expected to present any Brønsted acidity.

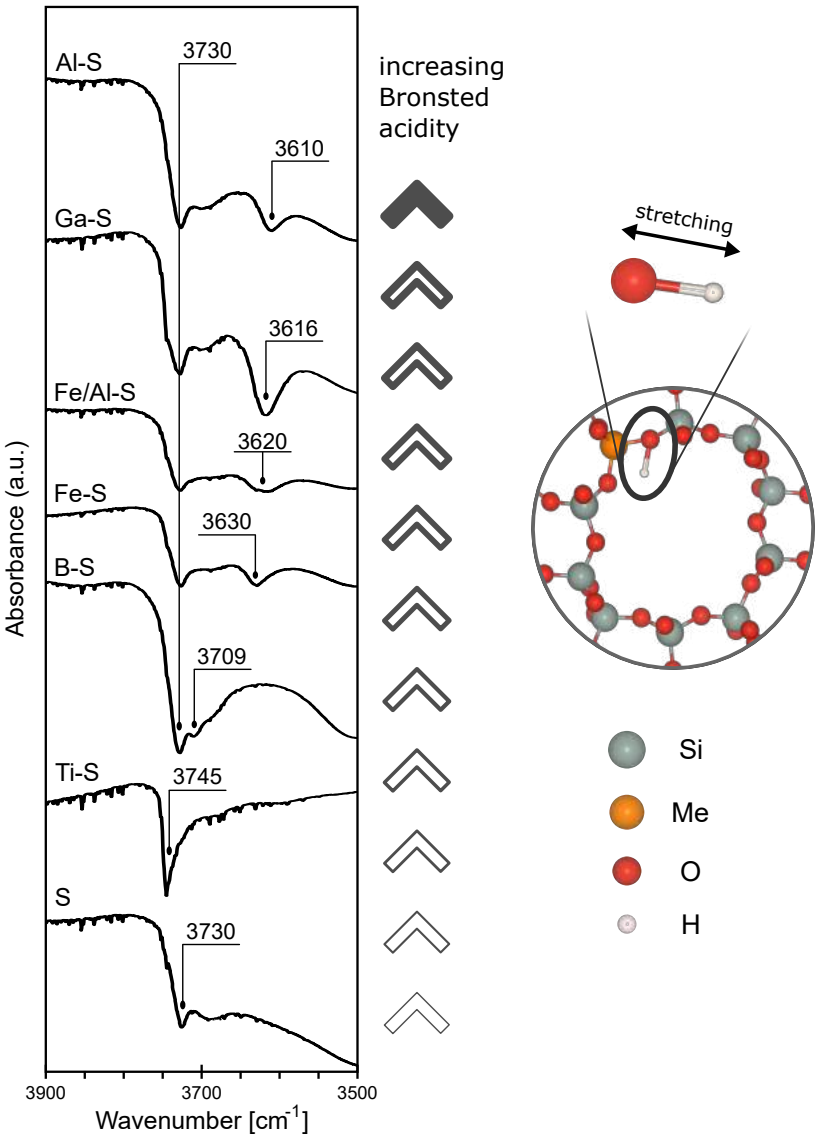

Figure 4.12: IR spectra recorded at room temperature in Ar of the calcined zeotype samples and schematic representation of the Brønsted acid sites and the O–H stretching vibration. Drawing produced by Vesta.[13]

Additional experiments were performed to further investigate the O−H stretching vibration region of the IR spectra of all samples and to confirm that the BASs are actually generated by the heteroatoms in framework position. Particular attention was given to Fe-S as nitrogen sorption, SEM and NO adsorption show the presence of Fe in extra framework position.

After exposing the samples to NH_3, the absorption peak assigned to the silanol groups and the BASs partially and completely disappears, respectively. As example, the IR spectra of Fe-S in the H^+-form before and after NH_3 adsorption are shown in Figure 4.13a. This indicates that some terminal ≡Si−OH remain intact whilst the BASs are totally substituted by ≡Si−O(NH_4)−Fe≡ species, confirming the stronger adsorption strength of the BASs compared to terminal ≡Si−OH. [21]

21: A complete assignment of the peaks of the entire spectra after NH_3 adsorption can be found in Paper I.

The IR spectra of Fe-S in the Na^+- and the NH_4^+-forms reported in Figure 4.13b and c do not show any peaks other than the peak assigned to the terminal −OH in the O−H stretching vibration region. These facts further confirm that in Fe-S some Fe is in framework position in place of Si and that the acidic properties discussed in this work are only related to the Fe incorporation in the zeotype structure. [22]

22: Indeed, if one speculates the presence of some Fe species other than framework species capable to influence the zeotype acidity, it is reasonable to assume that these Fe species are present already in the as synthesized material, or at least after the elimination of the organic template. Contrary, the −OH groups with acid properties are present only after the calcination of the zeotype in the NH_4^+-form.

An IR spectrum of the Fe-impregnated silicalite sample was recorded after O_2 pretreatment at room temperature in Ar to fully exclude the possibility that extra framework Fe species could influence the zeotype acidity (Figure 4.13d). Again, no peaks other than the peak assigned to the terminal silanol groups can be identified in this region.

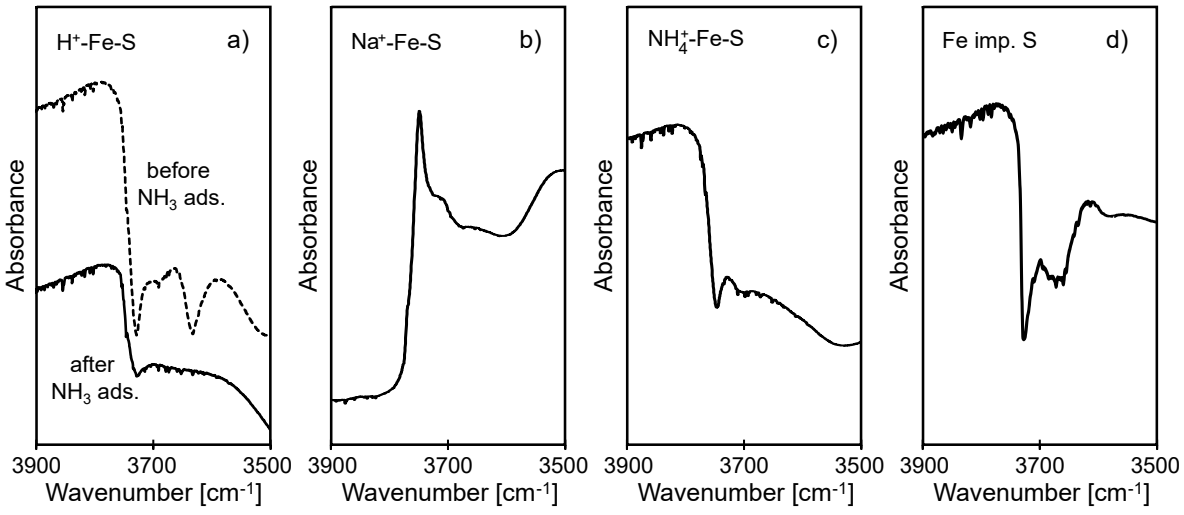

Figure 4.13: a) IR spectra recorded in Ar at room temperature before and after NH_3 adsorption on Fe-S in the H^+-form. b) Background subtracted IR spectrum of Fe-S after elimination of the SDA recorded at room temperature in Ar (the background was taken at 200 °C in 10% O_2/Ar). c) IR spectrum of Fe-S in the NH_4^+-form recorded at room temperature in Ar. d) IR spectrum of the Fe-impregnated silicalite sample recorded at room temperature in Ar after 1 h 10% O_2/Ar pretreatment at 500 °C.

Investigation of the Fe species in the Fe-silicalite sample

To further investigate the Fe species in the Fe-containing samples, NO adsorption experiments were performed with DRIFTS on Fe-S and Fe/Al-S (see Figure 4.14). [23] The doublet of absorption peaks at 1580 and 1615 cm^{-1} and the absorption peak at 2135 cm^{-1} are assigned to bridging and bidentate nitrates[69], and NO^+ species occupying cationic position in the microporous structure[70], respectively. The doublet of absorption peaks at 1580 and 1615 cm^{-1} suggests the presence of extra framework Fe species capable of oxidizing NO to NO_3^-, but further experiments should be performed to clarify the nature of these Fe species. The fact that the absorption peak at 2135 cm^{-1} can only be observed in the Al containing samples might be due to the higher acidity of the Al-BASs. [24]

23: The same experiments were performed on S and Al-S for comparison. The entire spectra are reported in the Supplementary Information of Paper I.

24: *i.e.* to the fact that the Al-BASs donate protons easier than the Fe-BASs in favor of NO^+ species.

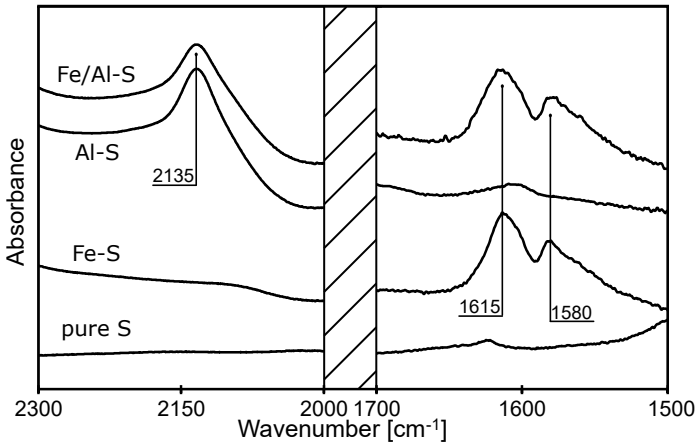

Figure 4.14: Background subtracted IR spectra recorded at room temperature in Ar after NO adsorption on S and Al-S, Fe-S and Fe/Al-S in the H^+-form. The background spectra were taken before each experiment at room temperature in Ar.

Further investigation of the Fe-exchanged samples with DRIFTS

In Figure 4.15 the O–H stretching region of the spectra of Ga-S in the H^+-form and after Fe-exchange is shown. With comparison to the absorption peak assigned to the Si–OH, the absorption peak at 3617 cm^{-1} assigned to the Ga-BASs decreases in intensity after Fe-exchange. Assuming that the Fe-exchange does not significantly affect the terminal silanol groups, this indicates the successful addition of Fe in ion-exchange position. However, the presence of the peak at 3617 cm^{-1} in the spectrum of Fe_{ex}-Ga-S suggests that some Brønsted acid sites are still present in the zeotype sample and, thus, that the ion-exchange was not complete. Similar results have been obtained after Fe-exchanging Al-S, B-S and Fe-S.

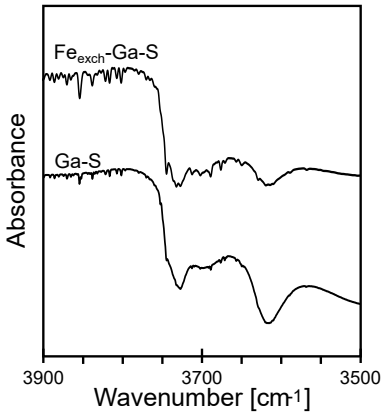

Figure 4.15: IR spectra recorded at room temperature in Ar of Ga-S and Fe_{ex}-Ga-S.

Take-home message

The *in situ* IR spectra collected during the elimination of the TPA^+ from the as synthesized samples showed that TPA^+ ions are enchlatrated in the MFI framework, functioning indeed as directing agents rather than organic templates. The IR spectra collected during the activation of the NH_4^+-form of the zeotypes showed that −OH groups with acidic properties are present when Si is isomorphically substituted by a metal with oxidation state +3 in the MFI framework. A series of increasing acidity could be outlined and further IR experiments confirmed that the acidity of the samples derives only from the metal in T position. That the intensity of the peak assigned to the BASs decreased after Fe-exchange of all samples confirmed the successful ion-exchange.

Ad-species during methanol-TPD and methane exposure with DRIFTS

5

5.1 Symmetry of methoxy groups

Temperature programmed desorption of CH_3OH and CH_4 exposure experiments followed by DRIFTS were performed in order to investigate two of the key steps in the direct conversion of methane to methanol, namely the extraction of CH_3OH and the activation of CH_4. To better understand the evolution of the methoxy *ad*-species, particular attention was given to the $-CH$ and the $-OH$ stretching regions of the spectra. Therefore, it can be helpful to shortly describe the symmetries of the vibration modes of the $-CH_3$ group to more clearly discuss the results from the CH_3OH-TPD and the CH_4 exposure experiments.

The symmetry of methyl groups ($-CH_3$) belongs to the rotational group *C* since there is only one rotational axis. Furthermore, in most chemical structures, the three $C-H$ bonds of a methyl group are equivalent and therefore the $-CH_3$ group has C_{3v} [1] type of symmetry [71]. Thus, a methyl group usually shows one symmetric and two degenerate antisymmetric $C-H$ stretching modes. In a free molecule of methanol, instead, the three $C-H$ bonds are not equivalent because of the contribution of the oxygen atom and therefore the $-CH_3$ group has C_S [2] type of symmetry. Thus, three absorption peaks are expected to be present in the $C-H$ stretching vibration region of the IR spectrum of CH_3OH: one for the symmetric, one for the out-of-plane antisymmetric and one for the in-plane antisymmetric $C-H$ stretching vibration. Therefore, the symmetry of the $-CH_3$ groups belonging to methoxy groups formed on adsorption sites in zeolites, and thus the number of relative absorption peaks, depends on the structure of the adsorption site and the surrounding local environment. [3] A schematic representation of the different types of symmetries of the methoxy groups adsorbed on adsorption sites, together with the molecule of methanol, is reported in Figure 5.1.

1: where $_3$ indicates that the order of the rotational axis is 3 and $_v$ indicates that there are only vertical mirror planes containing the main axis.

2: where $_S$ indicates that there is only one mirror plane.

3: Indeed, in previous studies, the absorption peaks assigned to the $C-H$ stretching vibrations of methoxy groups adsorbed on zeolites occur both in triplets and in doublets, depending on the type of adsorption site.

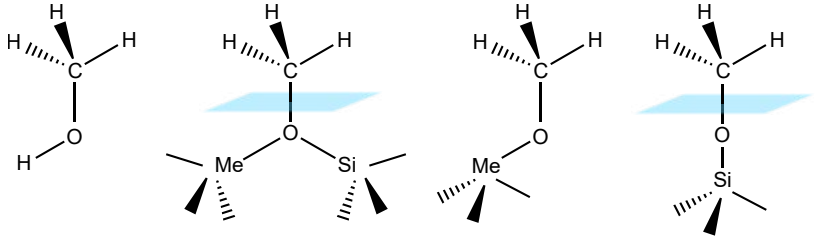

Figure 5.1: Schematic representation of the methanol molecule and methoxy groups adsorbed on BASs (Me = metal), other metal sites and terminal silanol groups (from left to right). The presence and the absence of the blue mirrors indicate the C_{3v} and the C_S type of symmetries, respectively, of the $-CH_3$ groups.

Take-home message

Methoxy groups show different symmetry depending on the adsorption site, and therefore different numbers of non-degenerate absorption bands are expected in the relative IR spectra.

5.2 Temperature programmed desorption of methanol with DRIFTS

In Figure 5.2 the complete spectral series of Ga-S collected during CH_3OH-TPD is shown. It is clear that the C–H and the O–H stretching regions are the most relevant in order to investigate the evolution of the surface species during the experiment. Therefore, particular attention will be given to these two regions for the spectral series of the other samples.

In Figure 5.3a, the C–H stretching region of the IR spectra of all samples recorded at 50, 250 and 450 °C after CH_3OH adsorption is shown. [4] It can be observed that the higher the acidity of the samples, the more intense are overall the absorption peaks in

4: For clarity, the IR spectra related to the intermediate temperature steps are not shown as they would not give additional information to the study. Furthermore, the spectral series of S and Fe/Al-S are not shown since the first shows similar features to B-S and the latter shows intermediate behavior between Fe-S and Al-S.

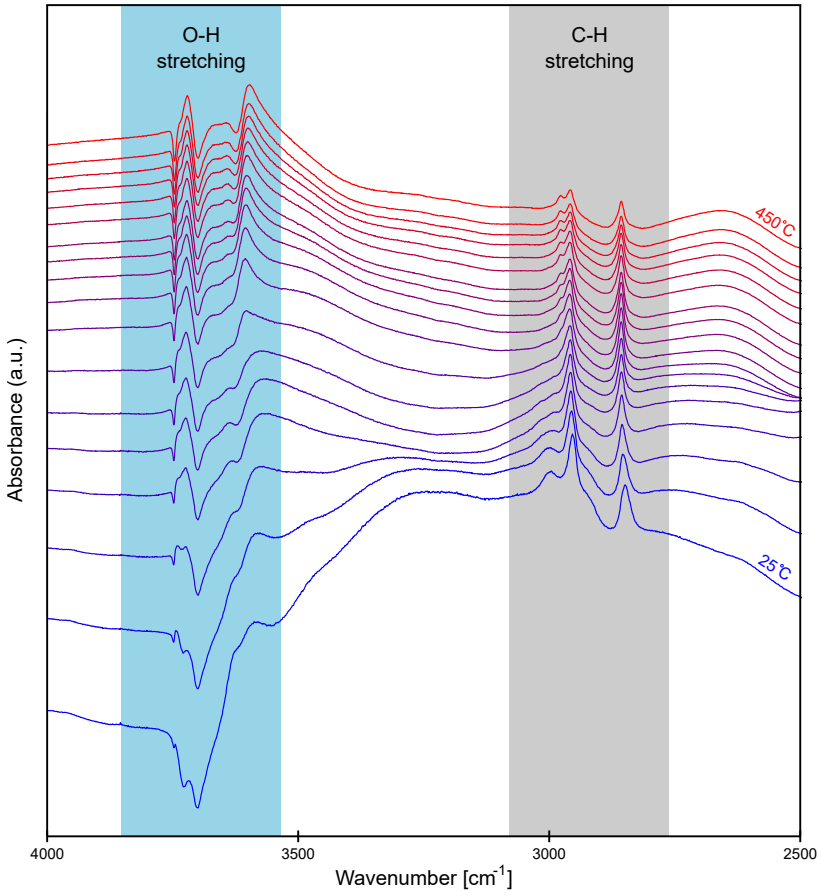

Figure 5.2: Complete background subtracted CH_3OH-TPD IR spectral series recorded in Ar from 25 to 450 °C (steps of 25 °C) of Ga-S in the H^+-form. The background spectrum was taken in Ar at room temperature after the 10% O_2/Ar pretreatment and before CH_3OH adsorption.

the IR spectra, and therefore the higher the adsorption strength of the samples towards the adsorbed species. In particular, the spectra of S and Ti-S show similar trends and absorption peaks with overall lower intensity. Indeed, both S and Ti-S have shown no Brønsted acidity, as revealed in Figure 4.12, and therefore they are not expected to have strong adsorption sites.

As mentioned in Section 5.1, liquid methanol shows methyl groups with C_S type of symmetry. Indeed, three absorption peaks at 2980, 2946 and 2834 cm^{-1} are observed in the C–H stretching region of the IR spectra of liquid methanol, which are assigned to the out-of-plane antisymmetric, the in-plane antisymmetric and the symmetric C–H stretching vibration, respectively [72]. At 50 °C, methanol is hydrogen bonded to the zeotype surface and the methyl groups have therefore a C_S type of symmetry as well. The absorption peaks for all samples in Figure 5.3a at 2998 and 2954, and 2852 cm^{-1} are thus assigned to the two antisymmetric and the symmetric C–H stretching vibrations of methanol hydrogen bonded to the zeotype surface. [5] The blueshift of the absorption peaks in the spectra of adsorbed CH_3OH in Figure 5.3a compared to liquid CH_3OH [72] is due to the interaction of the molecule with the zeotype surface and has previously been observed in the literature [74, 75].

As the temperature of the DRIFTS cell is increased, the physisorbed

5: Ti-S shows additional absorption peaks around 2930 and 2830 cm^{-1}. With regard to the first peak, a pronounced shoulder at 2930 cm^{-1} has previously been assigned to an overtone or a combination of the bending modes of the methoxy species belonging to methanol adsorbed at room temperature on pure silicalite [73]. To the authors' knowledge, no assignment has previously been done in the literature to absorption peaks around 2830 cm^{-1} for silicalite samples after CH_3OH adsorption. However, this peak markedly decreases in intensity as the temperature of the DRIFTS cell is increased, and ultimately disappears at 200 °C. It is thus reasonable to assume that the adsorbed species whose vibrations result in the peak around 2830 cm^{-1}, are not strongly bound to the surface of Ti-S.

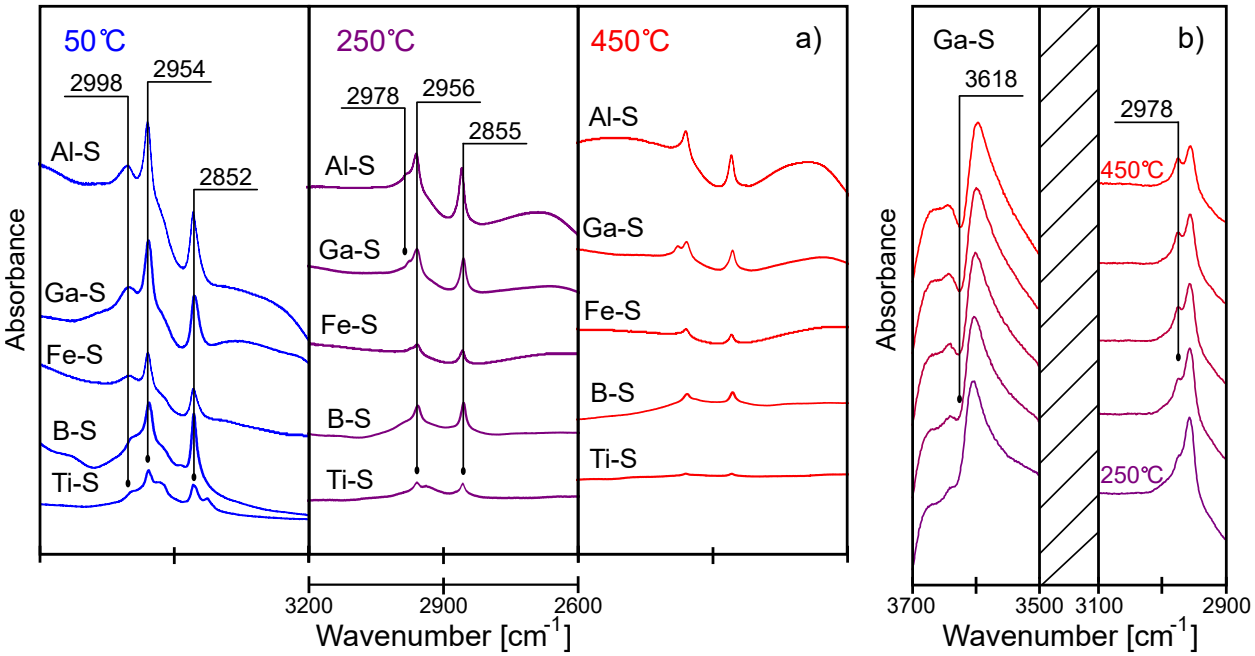

Figure 5.3: a) Background subtracted CH_3OH-TPD IR spectra recorded in Ar at 50, 300 and 550 °C of Al-S, B-S, Fe-S, Ga-S and Ti-S in the H^+-form. The background spectra were taken in Ar at room temperature after the 10% O_2/Ar pretreatment and before CH_3OH adsorption; b) Background subtracted CH_3OH-TPD IR spectral series recorded in Ar from 200 to 550 °C (steps of 50 °C) of Ga-S in the H^+-form. The background spectrum was taken in Ar at room temperature after the 10% O_2/Ar pretreatment and before CH_3OH adsorption.

methanol desorbs, leaving only the methoxy species that are more strongly bound to the zeotype adsorption sites. Two and three absorption peaks can be observed in the spectra of Ti-S, B-S and Fe-S, and in the spectra of Ga-S and Al-S, respectively. This suggests that methoxy groups are adsorbed on one type of adsorption site in Ti-S, B-S and Fe-S, and on two types of adsorption site in Ga-S and Al-S. [6] The absorption peaks at 2956 and 2855 cm^{-1}, in common for all samples, have previously been assigned to the antisymmetric and symmetric C−H stretching vibration of ≡Si−O(CH_3) species, respectively [46, 75]. Absorption peaks around 2980 cm^{-1} were previously observed after CH_3OH adsorption on Al-containing ZSM-5 zeolites. It is widely accepted that the latter absorption peak is assigned to the antisymmetric C−H vibration of methoxy groups strongly bound on BASs generated by Al after CH_3OH adsorption [75–78]. Furthermore, as it will be discussed in Section 5.3, an absorption peak at 2978 cm^{-1} is assigned to the antisymmetric C−H vibration of methoxy groups adsorbed on BASs generated by Fe after CH_4 exposure. Therefore, it seems that the type of metal which generates the BASs does not significantly influence the position of the peak assigned to the C−H stretching of the methoxy groups adsorbed on the BASs.

6: Assuming a C_{3v} type of symmetry of the adsorbed methoxy groups, two peaks are expected for each type of adsorption site (two degenerate for the antisymmetric and one for the symmetric C−H stretching vibrations).

Based on these considerations, the absorption peaks in the spectra of Ga-S and Al-S at 2978 cm^{-1} in Figure 5.3a are assigned to the antisymmetric C−H stretching of ≡Si−O(CH_3)−Al≡ and ≡Si−O(CH_3)−Ga≡ species, respectively. This assignment is further supported by Figure 5.3b, where the O−H and C−H stretching regions of the CH_3OH-TPD IR spectral series of Ga-S are shown with smaller temperature-steps than in Figure 5.3a. [7] As soon as the positive peak at 2978 cm^{-1} forms at around 250 °C, a negative peak at 3618 cm^{-1} forms as well, and these two peaks evolve together as the temperature of the DRIFTS cell is increased. Since the absorption peak at 3618 cm^{-1} was assigned to the O−H stretching vibration of Ga-BASs (Figure 4.12), Figure 5.3b clearly shows that methoxy groups become IR visible at the expenses of −OH groups belonging to Ga-BASs, confirming our assignment of the absorption peak at 2978 cm^{-1}. [8] It is noteworthy that B-S and Fe-S show no peaks other than the ones assigned to the C−H stretching vibration of ≡Si−O(CH_3), suggesting that B- and Fe-BASs are not strong adsorption sites towards CH_3OH.

7: The spectra of Al-S show similar behavior, but the negative absorption in the O−H stretching region is centered at 3610 cm^{-1}.

8: It should be noted that the intensities of the peaks at 2855 and 2956 cm^{-1}, on one side, and the intensity of the peak at 2978 cm^{-1}, on the other side, are generated by species that occur in different amounts in Ga-S and Al-S (Si/Al = Si/ Ga = 50). Furthermore, the peaks at 2855 and 2956 cm^{-1} clearly appear already at a lower temperature and decrease in intensity during the TPD experiments, whilst the peak at 2978 cm^{-1} appears only at higher temperatures. For these reasons, a direct comparison of the intensities of the aforementioned peaks might lead to misinterpretations. Therefore, we suggest that the formation of the peak at 2978 cm^{-1} at 250 °C and its disappearance at higher temperatures indicate the high adsorption strength of Ga- and Al-BASs towards methanol in the form of methoxy groups.

The IR spectra of Ga-S and Al-S are the only ones showing clear absorption peaks at 450 °C, indicating some methoxy groups are still adsorbed on the zeotype surface. B-S, Fe-S and Ti-S show absorption peaks with lower intensities, suggesting that most methoxy species are desorbed in the last step of the TPD experiments. That the spectrum of Ga-S shows the absorption peak at 2978 cm^{-1} and the spectrum of Al-S does not, is still unclear.

Indeed, as shown in Figure 4.12 and supported by the literature, the Ga-BASs are weaker than the Al-BASs, and therefore are expected to show weaker adsorption strength towards the methoxy groups. Therefore, further investigations should be done regarding this matter.

In Figure 5.4 the C−H stretching region of the IR spectra of Fe_{ex}-Ga-S recorded at 50, 250 and 450 °C after CH_3OH adsorption is shown. These spectra are very similar to the spectra of Ga-S recorded during CH_3OH-TPD (see Figure 5.3). Indeed, at 50 °C, the peaks at 2998, 2954 and 2852 cm^{-1} are assigned to the C−H stretching vibrations of CH_3OH hydrogen bonded to the zeotype surface. At 150 °C the absorption peaks at 2956 and 2855 cm^{-1} are assigned to the C−H stretching vibrations of $\equiv Si-O(CH_3)$ species. The presence of the absorption peak at 2978 cm^{-1} assigned to the C−H stretching vibrations of $=Si-O(CH_3)-Ga=$ species confirms that Fe_{ex}-Ga-S still shows BASs and that they are capable of binding CH_3OH as methoxy groups. At 450 °C, the spectrum shows still absorption peaks, indicating that methoxy groups are still adsorbed on the zeotype surface. Similar results have been obtained for Al-S, B-S, Fe-S, Fe/Al-S and Ti-S in the Fe-exchanged form. Therefore, further investigations on Fe-exchange samples should be done in order to better investigate the influence of the ion-exchange on CH_3OH-TPD experiments.

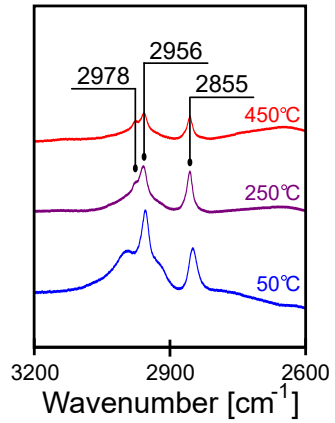

Figure 5.4: Background subtracted CH_3OH-TPD IR spectra recorded in Ar at 50, 250 and 450 °C of Fe_{ex}-Ga-S. The background spectrum were taken in Ar at room temperature after the 10% O_2/Ar pretreatment and before CH_3OH adsorption.

The IR spectra recorded during the CH_3OH-TPD experiments showed that the lower the acidity of the sample, the lower the overall adsorption strength towards methanol. Furthermore, methoxy groups are formed at high temperatures on BASs only in the samples showing stronger Brønsted acidity. This indicates that acidity is indeed a descriptor for CH_3OH desorption from zeotype surfaces. Further investigation should be done on the Fe-exchanged samples since no significant differences from the parent materials in the H^+-form could be observed.

5.3 Methane exposure with DRIFTS

CH_4 exposure experiments were performed to evaluate whether the samples are capable of adsorbing methane and therefore to gain knowledge on the CH_4 activation step in the direct conversion of methane to methanol. [9] The samples were also exposed to water to simulate the last step in the DCMM, *i.e.* the extraction of methanol using a solvent. Before exposing the samples to CH_4, the samples were pretreated in N_2O at 200 °C as it has been shown in literature that Fe-containing zeolites form active species towards the DCMM in these conditions. In this Section, the abbreviations

9: The CH_4 exposure experiments were performed only for S, Al-S, Fe-S and Fe/Al-S in the H^+-form. Indeed, they belong to the batch of samples I synthesized earlier in my doctoral studies, and therefore more time was available for a more extensive investigation of their properties. Further studies should be carried on B-S, Ga-S and Ti-S and the Fe-exchanged samples to obtain a more complete overall characterization.

Fe-BASs and Fe-*extra* will be used. Fe-BASs refers to Brønsted acid sites generated by Fe in the MFI framework. Fe-*extra* refers to iron species in extra-framework position present in the channels and cages of the zeotype. The latter iron sites are the result of the instability of the metal in the MFI framework, which therefore tends to migrate from framework to extra-framework position.

In Figure 5.5 the C–H stretching region of the spectra recorded after CH_4 and H_2O exposure are reported for S, Al-S, Fe-S and Fe/Al-S. [10] S and Al-S show no absorption peaks, meaning that these samples are not capable of activating CH_4. The Fe-containing samples, instead, show absorption bands in this region, indicating formation of methoxy groups on adsorption sites of the zeotype samples. The presence of four absorption bands in the C–H stretching region of the spectra of the Fe-containing samples suggests that methoxy groups are adsorbed on at least two different types of Fe-sites. Furthermore, Fe/Al-S shows generally less intense absorption peaks in this region compared to Fe-S, indicating that fewer methoxy groups are adsorbed on the adsorption sites. [11] This further confirms the inactivity of the Al sites of the Al-containing zeotype samples for CH_4 activation.

The assignment of the absorption peaks in the C–H stretching region of the spectra recorded after CH_4 exposure has been challenging. Other research groups have previously performed CH_4 exposure experiments followed by IR spectroscopy on Fe-containing zeolites [44, 76, 79]. However, although there are some similarities between those studies and the study described here, [12] the activation of CH_4 by zeotypes with Fe incorporated in the MFI framework has not been investigated in the literature to my knowledge, and therefore the absorption peaks of Figure 5.5 represent a novelty in the field. As shown in Figure 5.5, four absorption peaks in the spectra of the Fe-containing samples appear after CH_4 exposure,

10: The IR spectra recorded after 30 minutes of CH_4 exposure are not shown as they would not give additional information to the study. The background subtracted spectra recorded in Ar before exposing the samples to CH_4 are also reported to confirm the absence of impurities, which could mislead the interpretation of the spectra.

11: Indeed, Fe-S contains twice the amount of Fe than Fe/Al-S and therefore it is reasonable that the latter shows lower activity for CH_4 activation.

12: In those studies, CH_4 activation by zeolites where Fe is not incorporated in the MFI framework was investigated.

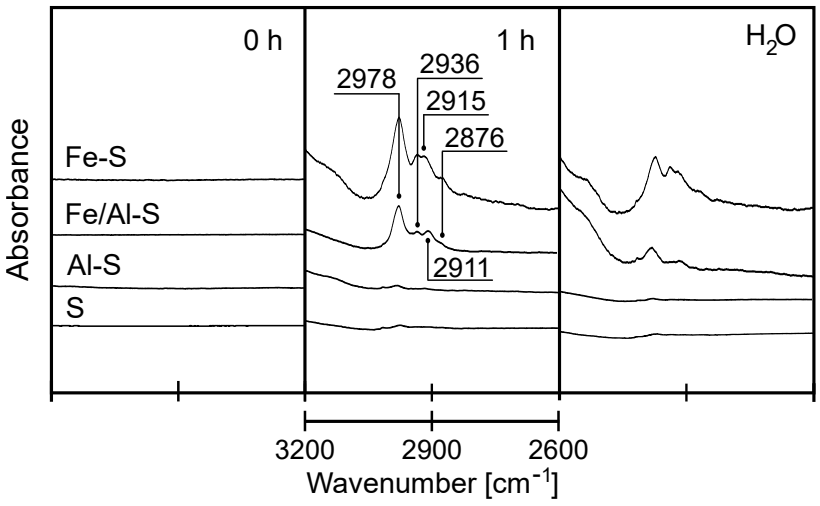

Figure 5.5: Background subtracted IR spectra recorded at 250 °C in Ar after exposing S, Al-S, Fe-S and Fe/Al-S in the H^+-form to 2% CH_4/Ar at 250 °C for 0 and 1 hours and to 4% H_2O/Ar at 250 °C for 30 minutes. The background spectra were taken in Ar at 250 °C after the pretreatment in 500 ppm N_2O/Ar and before CH_4 exposure.

centered at 2978, 2936, 2915 and 2876 cm^{-1}. Other research groups have previously assigned peaks at 2964 and 2920, and 2823 cm^{-1} to the two antisymmetric and the symmetric C−H stretching vibration of methoxy groups adsorbed on N_2O-activated Fe-containing zeolites upon methane exposure. In order to follow these results from previous literature, the rationale for the assignment of the absorption peaks in Figure 5.5 is built on the following:

- Methoxy groups are the most likely species formed upon CH_4 exposure on the Fe-containing silicalite samples; [13]
- Methoxy groups are formed only on Fe-species in the Fe-containing samples; [14]
- The Fe-BASs and the Fe-*extra* sites are the most plausible adsorption sites for the methoxy groups. Indeed, it was shown that some Fe is in framework position in Fe-S and Fe/Al-S and it is shown in literature that Fe-zeolites show the formation of Fe-*extra* upon N_2O exposure;
- Five vibration modes, and thus five distinct absorption peaks in the C−H stretching region of the spectra of Fe-S and Fe/Al-S of Figure 5.5, are expected: one symmetric and two antisymmetric for the Fe-*extra*, [15] and one symmetric and two degenerate antisymmetric for the Fe-BASs [16].

13: This is supported in literature by the fact that Fe-containing zeolites and zeotypes have predominantly shown formation of methoxy groups upon CH_4 exposure experiments.

14: This is supported by the absence of any absorption peaks in the C−H stretching region of the spectra collected after CH_4 exposure of S and Al-S.

15: Previous research groups assign one symmetric and two antisymmetric vibrations for the C−H stretching of methoxy groups adsorbed on Fe-*extra* sites. The latter suggests a C_S type of symmetry of the $-CH_3$ groups belonging to the methoxy groups adsorbed on Fe-*extra* sites. This is further confirmed by the reaction sequence (proposed in [76] and supported by DFT calculations in [80]) for the formation of methoxy species on Fe sites during the oxidation of CH_4 by N_2O.

16: As seen in in the previous Section, it is well established that methoxy groups adsorbed on BASs show C_{3v} type of symmetry.

Based on these considerations, the absorption peaks at 2978 and 2876 cm^{-1} in Figure 5.5 are assigned to the antisymmetric and symmetric C−H stretching vibrations of methoxy groups adsorbed on Fe-BASs. This is the most plausible assignment since:

- Absorption peaks in these positions have not been observed for Fe-containing zeolite samples where Fe is in extra-framework position, upon CH_4 exposure;
- Adsorption of methoxy groups on Fe-BASs has not been investigated in literature before, to my knowledge;
- Absorption peaks centered at 2978 and 2867 cm^{-1} have previously been assigned to the antisymmetric and symmetric C−H stretching vibrations of methoxy groups adsorbed on Al-BASs.

The negative absorption peak at 3630 cm^{-1} for Fe-S (see Figure 5.6) further confirms this assignment. Indeed, it was shown in Figure 4.12 that the O−H stretching vibration of the Fe-BASs in Fe-S results in an absorption peak centered at 3630 cm^{-1}. Therefore, the aforementioned peak in Figure 5.6 suggests the loss of −OH groups belonging to Fe-BASs in favor of the adsorption of methoxy groups.

The absorption peaks centered at 2936 and 2915 cm^{-1} in the spectra of Figure 5.5 are assigned to the antisymmetric C−H stretching vibrations of methoxy groups adsorbed on Fe-*extra* sites.

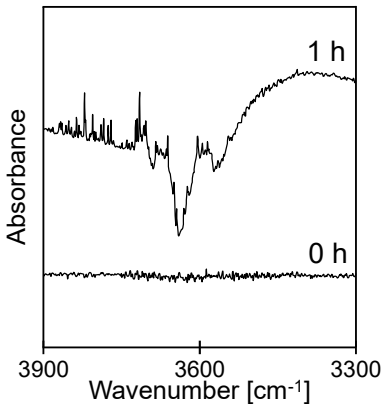

Figure 5.6: O–H stretching region of the background subtracted IR spectra recorded at 250 °C in Ar after exposing Fe-S in the H^+-form to 2% CH_4/Ar at 250 °C for 0 and 1 hours. The background spectrum was taken in Ar at 250 °C after the pretreatment in 500 ppm N_2O/Ar and before CH_4 exposure.

17: Indeed, it is not unusual that the relative intensities of absorption peaks in IR spectroscopy differ from diffuse reflectance and transmittance mode [81].

18: It should also be noted that the absorption peak centered at 2978 cm^{-1} is the most pronounced and intense of the quadruplet in the spectra of Figure 5.5 after 1 h of CH_4 exposure. Therefore, it is reasonable to assume that there are more Fe-BASs where methoxy groups are adsorbed than Fe-*extra* sites. In this perspective, Fe-BASs seem to act as efficient methoxy-storage sites once CH_4 is activated by the Fe-*extra*.

The relative symmetric vibration might be covered by the other vibrations whose absorption peaks are adjacent in the spectra, *e.g.* the peak assigned to the symmetric C–H stretching vibration of the methoxy groups adsorbed on Fe-BASs. A possible explanation is the different IR setup used in this study compared to the one used in the previous literature. [17] Furthermore, since the structure of the Fe-*extra* active towards CH_4 activation is still under debate, I do not exclude the possibility that the methoxy groups adsorbed on Fe-*extra* sites show a C_{3v} type of symmetry. In the latter case, the absorption peaks centered at 2936 and 2915 cm^{-1} in Figure 5.5 could be assigned to the antisymmetric and symmetric C–H stretching vibrations of methoxy groups adsorbed on Fe-*extra* sites.

Regarding the role of the different Fe sites during the CH_4 exposure experiments, that the Fe-BASs are active towards CH_4 dissociative adsorption and partial oxidation is unlikely. Following also previous literature, it is, instead, likely that only Fe-*extra* are active towards CH_4 activation. In this case, the Fe-BASs would solely aid as adsorption sites for methoxy groups previously formed on Fe-*extra* sites. [18] Moreover, it is noteworthy that the intensities of all absorption peaks decrease after H_2O exposure, suggesting that some methoxy groups are protonated and desorb from the adsorption sites of the zeotype samples. A more pronounced decrease of the intensity of the absorption peak centered at 2978 cm^{-1} after H_2O exposure compared to the absorption peak centered at 2936 cm^{-1} is observed. Therefore, one could speculate on the higher adsorption strength of the Fe-*extra* sites towards CH_4 and the more facile desorption of the methoxy groups during H_2O exposure from the Fe-BASs.

Take-home message

In the CH_4 exposure experiments, absorption peaks could only be observed in the spectra of Fe-S and Fe/Al-S, suggesting that the presence of Fe promotes CH_4 activation. The assignment of the peaks led to the conclusion that methane is activated by extra-framework Fe species, and eventually further adsorbed on the Fe-BASs.

6 Concluding remarks

6.1 What have I shown?

Silicalite zeotypes with the MFI framework have been synthesized with Al, B, Fe, Ga and Ti in framework position. A pure silicalite sample, *i.e.* only with Si and O, have been prepared for comparison. The SEM and TEM images have shown high crystallinity of all prepared zeotype samples, and that the use of different metal precursors has led to some differences in the crystals morphology. XRD confirmed that all samples show the MFI type of framework structure. The microporous structure is further confirmed by N_2 sorption, that gave additional information about metal incorporation. Polarized Raman spectroscopy allowed to clarify previous assignments found in the literature of some peaks related to the *n*-membered rings of the MFI framework and to speculate on the position of the Brønsted acid sites in the Al-silicalite sample.

A delay between the elimination of the structure directing agent and the formation of CO_2 as its ultimate combustion product has been observed in the IR spectral series recorded during the removal of the organic molecule by calcination from the zeotype framework of the as synthesized samples. This fact suggests that the TPA^+ ions first lose contact with the internal surface of the zeotype as consequence of the breakage of the Van der Waals interactions, and then at higher temperature are oxidized to CO_2. The simultaneous disappearance of $-NH$ species and appearance of acid $-OH$ species in the IR spectral series recorded during calcination of the NH_4^+-form of the zeotype samples suggest the assignments of the latter peaks to the $O-H$ stretching vibration of the Brønsted acid sites of the zeotypes. The absence of any acidic $-OH$ groups in the zeotype samples both in the Na^+- and NH_4^+-forms and in the Fe-impregnated silicalite sample, and the NH_3 adsorption experiments confirm this assignment. Therefore the following series of increasing acidity could be outlined: 0 = pure silicalite = Ti-silicalite < B-silicalite < Fe-silicalite < Fe/Al-silicalite < Ga-silicalite < Al-silicalite. That the intensity of the peak assigned to the BASs has decreased after Fe-exchange of all samples has confirmed the successful ion-exchange.

The IR spectra recorded during the temperature programmed desorption of methanol has shown that the lower the acidity of the sample, the lower the overall adsorption strength towards methanol. Furthermore, methoxy groups are formed at high temperatures on BASs only in the samples showing stronger Brønsted acidity. This indicates that the acidity is indeed a descriptor for CH_3OH desorption from zeotype surfaces. Further investigation should be done on the Fe-exchanged samples since no significant differences from the parent materials in the H^+-form could be observed. In the methane exposure experiments, absorption peaks could only be observed in the spectra of the samples where Fe was added in the MFI framework, suggesting that the presence of Fe promotes CH_4 activation.

The assignment of the peaks has led to the conclusion that methane is likely activated by extra-framework Fe species, and eventually further adsorbed on the Fe-BASs.

In conclusion, the ultimate goal of this study was to design a model catalyst for the direct conversion of methane to methanol (DCMM). In this perspective, zeotypes with custom-made properties have been synthesized and characterized with various techniques. By making use of the prepared materials, the entangled DCMM reaction has been unraveled to more easily accessible experiments to pinpoint the catalyst design principles needed for this reaction. We have shown that aluminum-free zeotypes containing iron are promising catalysts for the DCMM reaction, and that the acidity of the material is a descriptor for methanol desorption.

6.2 What next?

Further investigations of the zeotype samples prepared in this work shall be performed. About the materials characterization, polarized Raman spectroscopy would give additional information about the position of the BASs generated by B and Ga, and maybe about the position of Ti in the MFI framework. Calorimetry and NH_3-adsorption experiments would help to better understand the addition of the metals in the framework and to make quantitative analyses of the acidity of the zeotype samples. About the DCMM, methane exposure experiments shall be performed on the Fe-exchanged silicalite samples to investigate the synergy of Fe in ion-exchange position and BASs with tuned acidity. Furthermore, a deeper analysis of the CH_3OH-TPD experiments on the Fe-exchanged samples shall be carried.

On-going experiments involve the synthesis of zeotypes with the MFI framework with other metals in framework position (*i.e.* La, Ce, Y, Sc and Mg). These samples shall be characterized to confirm the microporous structure and the incorporation of the metals in the framework. The idea is to further extend the zeotype series with tuned acidity and thus obtain a better understanding of the influence of the acidity on the direct conversion of methane to methanol.

Funding

This work was performed in part at the Chalmers Materials Analysis Laboratory, CMAL. The work was financially supported by the Swedish Research Council through the Röntgen-Ångström collaborations "Time-resolved *in situ* methods for design of catalytic sites within sustainable chemistry" (No.349-2013-567), the Knut and Alice Wallenberg foundation "Atomistic design of catalysts" (No.2015.0058), and the Competence Centre for Catalysis, which is hosted by Chalmers University of Technology and financially supported by the Swedish Energy Agency (No. 22490-4) and the member companies AB Volvo, ECAPS AB, Johnson Matthey AB, Preem AB, Scania CV AB, Umicore Denmark ApS and Volvo Car Corporation AB. A.M. and S.V. acknowledge funding from the Swedish Foundation for Strategic Research (SSF, FFL-6 program, grant no FFL15-0092) and from the Knut and Alice Wallenberg Foundation (Academy Fellows program, grant no 2016-0220).

Bibliography

[1] A.F. Cronstedt and Kemiska AB Candor. *Rön och försök gjorde med en malm-art, från Los' Kobolt grufvor i Färila socken och Helsingeland: ur Kungl. Vetenskapsakademiens handlingar 1751*. utg., 1756 (cit. on pp. 1, 3).

[2] H de Sainte Claire Deville and HJ Debray. 'Comptes Rendus Acad'. In: *Sci* 54 (1862), p. 324 (cit. on p. 1).

[3] S Davis and Y Inoguchi. 'CEH Marketing Research Report: Zeolites'. In: *SRI Consulting* (2009) (cit. on p. 1).

[4] Ch Baerlocher, Lynne B McCusker and David H Olson. *Atlas of zeolite framework types*. Elsevier, 2007 (cit. on p. 1).

[5] Jiří Čejka et al. 'Zeolite-based materials for novel catalytic applications: Opportunities, perspectives and open problems'. In: *Catalysis Today* 179.1 (2012). The 4th Czech-Italian-Spanish (CIS-4) workshop on Molecular Sieves and Catalysis, pp. 2–15. DOI: https://doi.org/10.1016/j.cattod.2011.10.006 (cit. on p. 1).

[6] S Abate et al. 'Disruptive catalysis by zeolites'. In: *Catalysis Science & Technology* 6 (2016), pp. 2485–2501. DOI: 10.1039/C5CY02184G (cit. on p. 1).

[7] William Taifan and Jonas Baltrusaitis. 'CH4 conversion to value added products: Potential, limitations and extensions of a single step heterogeneous catalysis'. In: *Applied Catalysis B: Environmental* 198 (2016), pp. 525–547. DOI: 10.1016/j.apcatb.2016.05.081 (cit. on pp. 1, 10).

[8] Thomas J Lawton and Amy C Rosenzweig. 'Methane-oxidizing enzymes: an upstream problem in biological gas-to-liquids conversion'. In: *Journal of the American Chemical Society* 138.30 (2016), pp. 9327–9340 (cit. on p. 1).

[9] Virta R.L. *Survey Mineral Yearbook, 2008*. Vol. 83. Zeolites U.S. Geolog., 2008 (cit. on p. 3).

[10] Jiri Cejka and Herman van Bekkum. *Zeolites and ordered mesoporous materials: progress and prospects: the 1st FEZA School on Zeolites, Prague, Czech Republic, August 20-21, 2005*. Vol. 157. Gulf Professional Publishing, 2005 (cit. on p. 3).

[11] Lesley E.Smart Elaine and Elaine A.Moore. *Solid State Chemistry: An Introduction*. 2005, p. 486 (cit. on p. 3).

[12] Walter Loewenstein. 'The distribution of aluminum in the tetrahedra of silicates and aluminates'. In: *American Mineralogist* 39.1-2 (Feb. 1954), pp. 92–96 (cit. on p. 3).

[13] Koichi Momma and Fujio Izumi. 'VESTA 3 for three-dimensional visualization of crystal, volumetric and morphology data'. In: *Journal of Applied Crystallography* 44 (2011), pp. 1272–1276. DOI: 10.1107/S0021889811038970 (cit. on pp. 4, 5, 8, 33).

[14] H Van Bekkum et al. *Introduction to Zeolite Science and Practice*. 2001, pp. 633–671 (cit. on p. 3).

[15] Ferenc Lónyi and József Valyon. 'On the interpretation of the NH3-TPD patterns of H-ZSM-5 and H-mordenite'. In: *Microporous and Mesoporous Materials* 47.2-3 (2001), pp. 293–301. DOI: 10.1016/S1387-1811(01)00389-4 (cit. on p. 4).

[16] H. Berndt et al. 'Comparison of the acidic properties of ZSM-5 zeolites isomorphously substituted by Ga, In, B and Fe'. In: *Microporous Materials* 2.3 (1994), pp. 197–204. DOI: 10.1016/0927-6513(93)E0053-J (cit. on p. 4).

[17] R. B. Borade. 'Synthesis and characterization of ferrisilicate zeolite of pentasil group'. In: *Zeolites* 7.5 (1987), pp. 398–403. DOI: 10.1016/0144-2449(87)90003-0 (cit. on p. 4).

[18] Cynthia T W Chu et al. 'Isomorphous substitution in zeolite frameworks. II. Catalytic properties of [B]ZSM-5'. In: *Journal of Catalysis* 93.2 (1985), pp. 451–458. DOI: 10.1016/0021-9517(85)90192-7 (cit. on p. 4).

[19] G. Mul et al. 'NO adsorption on ex-framework [Fe, X]MFI catalysts: Novel IR bands and evaluation of assignments'. In: *Catalysis Letters* 80.3-4 (2002), pp. 129–138. DOI: 10.1023/A:1015456308687 (cit. on p. 4).

[20] Kuei-Jung Chao et al. 'Single crystal structure refinement of TPA ZSM-5 zeolite'. In: *Zeolites* 6.1 (1986), pp. 35–38. DOI: 10.1016/0144-2449(86)90009-6 (cit. on p. 4).

[21] E. M. Flanigen et al. 'Silicalite, a new hydrophobic crystalline silica molecular sieve.' In: *Nature* 271.5645 (1978), pp. 512–516. DOI: 10.1038/271512a0 (cit. on pp. 4, 26).

[22] R Szostak and TL Thomas. 'Crystallization of ferrisilicate molecular sieves with a sodalite structure'. In: *Journal of the Chemical Society, Chemical Communications* 2 (1986), pp. 113–114 (cit. on p. 6).

[23] Sandra L Burkett and Mark E Davis. 'Mechanisms of Structure Direction in the Synthesis of Pure-Silica Zeolites. 1. Synthesis of TPA/Si-ZSM-5'. In: *Chemistry of Materials* 1 (1995), pp. 920–928. DOI: 10.1021/cm00053a017 (cit. on p. 6).

[24] J. Cihlář. 'Hydrolysis and polycondensation of ethyl silicates. 1. Effect of pH and catalyst on the hydrolysis and polycondensation of tetraethoxysilane (TEOS)'. In: *Colloids and Surfaces A: Physicochemical and Engineering Aspects* 70.3 (1993), pp. 239–251. DOI: 10.1016/0927-7757(93)80298-S (cit. on p. 6).

[25] Manuel Moliner, Fernando Rey and Avelino Corma. 'Towards the rational design of efficient organic structure-directing agents for zeolite synthesis'. In: *Angewandte Chemie - International Edition* 52.52 (2013), pp. 13880–13889. DOI: 10.1002/anie.201304713 (cit. on p. 6).

[26] Sandra L Burkett and Mark E Davis. 'Mechanism of Structure Direction in the Synthesis of Pure-Silica Zeolites. 2. Hydrophobic Hydration and Structural Specificity'. In: *Chemistry of Materials* 7.2 (1995), pp. 1453–1463. DOI: 10.1021/cm00056a009 (cit. on p. 6).

[27] Rosemarie Szostak, Vinayan Nair and Tudor L Thomas. 'Incorporation and Stability of Iron in Molecular -sieve Structures'. In: (1987), pp. 487–494 (cit. on p. 7).

[28] Sandra L Burkett and Mark E Davis. 'Mechanism of Structure Direction in the Synthesis of Si-ZSM-5: An Investigation by Intermolecular 1H-29Si CP MAS NMR'. In: *J. Phys. Chem.* 98.Copyright (C) 2012 American Chemical Society (ACS). All Rights Reserved. (1994), pp. 4647–4653. DOI: 10.1021/j100068a027 (cit. on p. 7).

[29] Takaaki Ikuno et al. 'Structure-Directing Behaviors of Tetraethylammonium Cations toward Zeolite Beta Revealed by the Evolution of Aluminosilicate Species Formed during the Crystallization Process'. In: *Journal of the American Chemical Society* 137.45 (2015), pp. 14533–14544. DOI: 10.1021/jacs.5b11046 (cit. on p. 7).

[30] Donald W Breck. *Zeolite molecular sieves: structure, chemistry and use*. Krieger, 1984 (cit. on p. 7).

[31] JL Casci and CS Cundy. 'RM Barrer Hydrothermal Chemistry of Zeolites. Academic Press, London and New York'. In: *Clay Minerals* 18.2 (1983), pp. 223–223 (cit. on p. 7).

[32] CS Cundy. 'R. Szostak Molecular Sieves: Principles of Synthesis and Identification. Van Nostrand Reinhold, New York, 1989. 524 pp. Price£ 53.95.' In: *Clay Minerals* 25.2 (1990), pp. 244–244 (cit. on p. 7).

[33] Julian R Goldsmith. 'Synthetic soda-free thomsonite'. In: *Mineralogical Magazine and Journal of the Mineralogical Society* 29.218 (1952), pp. 952–954 (cit. on p. 7).

[34] Frank Albert Cotton, Geoffrey Wilkinson et al. *Advanced inorganic chemistry*. Vol. 6. Wiley New York, 1988 (cit. on p. 9).

[35] Giuseppe Etiope and Barbara Sherwood Lollar. 'ABIOTIC METHANE ON EARTH'. In: *Reviews of Geophysics* 51.2 (2013), pp. 276–299. DOI: 10.1002/rog.20011 (cit. on p. 9).

[36] W Liss. 'Addressing the challenges along the shale gas supply chain'. In: *Chem Eng Prog* (2012), p. 34 (cit. on p. 9).

[37] Evgenii V. Kondratenko et al. 'Methane conversion into different hydrocarbons or oxygenates: current status and future perspectives in catalyst development and reactor operation'. In: *Catal. Sci. Technol.* 7.2 (2017), pp. 366–381. DOI: 10.1039/C6CY01879C (cit. on pp. 9, 11).

[38] Pirnie Malcolm. *Evaluation of the fate and transport of methanol in the environment*. 1999 (cit. on p. 9).

[39] Claire Turner, Patrik Španěl and David Smith. 'A longitudinal study of methanol in the exhaled breath of 30 healthy volunteers using selected ion flow tube mass spectrometry, SIFT-MS'. In: *Physiological measurement* 27.7 (2006), p. 637 (cit. on p. 9).

[40] Jack H Lunsford. 'Catalytic conversion of methane to more useful chemicals and fuels: a challenge for the 21st century'. In: *Catalysis Today* 63.2 (2000), pp. 165–174. DOI: https://doi.org/10.1016/S0920-5861(00)00456-9 (cit. on p. 10).

[41] Zakaria and Kamarudin. 'Direct conversion technologies of methane to methanol: An overview'. In: *Renewable and Sustainable Energy Reviews* 65 (2016), pp. 250–261. DOI: 10.1016/j.rser.2016.05.082 (cit. on p. 10).

[42] T. L. Cottrell. *The Strengths of Chemical Bonds*. 2d ed., Bu. 1958 (cit. on p. 10).

[43] Gennady I. Panov et al. 'Generation of active oxygen species on solid surfaces. Opportunity for novel oxidation technologies over zeolites'. In: *Catalysis Today* 41.4 (1998), pp. 365–385. DOI: 10.1016/S0920-5861(98)00026-1 (cit. on p. 11).

[44] Eugeny V. Starokon et al. 'Room-temperature oxidation of methane by α-oxygen and extraction of products from the FeZSM-5 surface'. In: *Journal of Physical Chemistry C* 115.5 (2011), pp. 2155–2161. DOI: 10.1021/jp109906j (cit. on pp. 11, 42).

[45] Nadzeya V. Beznis, Bert M. Weckhuysen and Johannes H. Bitter. 'Partial Oxidation of Methane Over Co-ZSM-5: Tuning the Oxygenate Selectivity by Altering the Preparation Route'. In: *Catalysis Letters* 136.1 (May 2010), pp. 52–56. DOI: 10.1007/s10562-009-0206-6 (cit. on p. 11).

[46] Mayfair C. Kung, Sean S. -Y. Lin and Harold H. Kung. 'In situ Infrared Spectroscopic Study of CH4 Oxidation Over Co–ZSM-5'. In: *Topics in Catalysis* 55.1-2 (2012), pp. 108–115. DOI: 10.1007/s11244-012-9774-6 (cit. on pp. 11, 40).

[47] Yuni Krisyuningsih Krisnandi et al. 'Partial Oxidation of Methane to Methanol over Heterogeneous Catalyst Co/ZSM-5'. In: *Procedia Chemistry* 14 (2015). 2nd Humboldt Kolleg in conjunction with International Conference on Natural Sciences 2014, HK-ICONS 2014, pp. 508–515. DOI: https://doi.org/10.1016/j.proche.2015.03.068 (cit. on p. 11).

[48] Ceri Hammond et al. 'Direct catalytic conversion of methane to methanol in an aqueous medium by using copper-promoted Fe-ZSM-5'. In: *Angewandte Chemie - International Edition* 51.21 (2012), pp. 5129–5133. DOI: 10.1002/anie.201108706 (cit. on p. 11).

[49] By Stephen Brunauer, P H Emmett and Edward Teller. 'Adsorption of Gases in Multimolecular Layers'. In: *Journal of the American Chemical Society* 60.lc (1938), pp. 309–319. DOI: 10.1021/ja01269a023 (cit. on p. 15).

[50] Dung Van Vu et al. 'Catalytic activities and structures of silicalite-1 / H-ZSM-5 zeolite composites'. In: *MIcroporous and Mesoporous Materials* 115 (2008), pp. 106–112. DOI: 10.1016/j.micromeso.2007.12.034 (cit. on p. 23).

[51] Ch. Baerlocher and L.B. McCusker. *Database of Zeolite Structures*. http://www.iza-structure.org (cit. on p. 26).

[52] Pavol Hudec et al. 'Collect. Czech. Chem. Commun. (Vol. 63) (1998)'. In: 63 (1998) (cit. on p. 26).

[53] B Y R D Shannon et al. 'Revised Effective Ionic Radii and Systematic Studies of Interatomie Distances in Halides and Chaleogenides Central Research and Development Department , Experimental Station , E . L Du Pont de Nemours The effective ionic radii of Shannon & Prewitt [Acta'. In: *Acta Cryst.* A32 (1976), pp. 751–767 (cit. on p. 26).

[54] Matthias Thommes et al. 'Physisorption of gases, with special reference to the evaluation of surface area and pore size distribution (IUPAC Technical Report)'. In: *Pure and Applied Chemistry* 87.9-10 (2015), pp. 1051–1069. DOI: 10.1515/pac-2014-1117 (cit. on p. 27).

[55] Zeid A. Alothman. 'A review: Fundamental aspects of silicate mesoporous materials'. In: *Materials* 5.12 (2012), pp. 2874–2902. DOI: 10.3390/ma5122874 (cit. on p. 27).

[56] Matthias Thommes. 'Physical adsorption characterization of nanoporous materials'. In: *Chemie-Ingenieur-Technik* 82.7 (2010), pp. 1059–1073. DOI: 10.1002/cite.201000064 (cit. on p. 27).

[57] U. Mailer and in K.K. Unger K.K Unger. *Characterization of Porous Solid*. Elsevier, 1988, p. 101 (cit. on p. 28).

[58] Akira Saito and Henry C. Foley. 'High-resolution nitrogen and argon adsorption on ZSM-5 zeolites: effects of cation exchange and Si Al ratio'. In: *Microporous Materials* 3.4-5 (1995), pp. 543–556. DOI: 10.1016/0927-6513(94)00064-3 (cit. on p. 28).

[59] V. A. Maroni. 'Analysis of the Vibrational Characteristics of Zeolites Using Factor Group Methods.' In: *Applied Spectroscopy* 42.3 (1988), pp. 487–493. DOI: 10.1366/0003702884428077 (cit. on p. 29).

[60] Prabir K. Dutta, D. C. Shieh and M. Puri. 'Correlation of framework Raman bands of zeolites with structure'. In: *Zeolites* 8.4 (1988), pp. 306–309. DOI: 10.1016/S0144-2449(88)80127-1 (cit. on p. 29).

[61] A. J.M. de Man and R. A. van Santen. 'The relation between zeolite framework structure and vibrational spectra'. In: *Zeolites* 12.3 (1992), pp. 269–279. DOI: 10.1016/S0144-2449(05)80295-7 (cit. on p. 29).

[62] Yi Yu et al. 'Characterization of aluminosilicate zeolites by UV Raman spectroscopy'. In: *Microporous and Mesoporous Materials* 46.1 (2001), pp. 23–34. DOI: 10.1016/S1387-1811(01)00271-2 (cit. on p. 29).

[63] B. Hehlen. 'Inter-tetrahedra bond angle of permanently densified silicas extracted from their Raman spectra'. In: *Journal of Physics Condensed Matter* 22.2 (2010). DOI: 10.1088/0953-8984/22/2/025401 (cit. on p. 29).

[64] Pierre Bräuer et al. 'Effect of Al content on number and location of hydroxyl acid species in zeolites: A DRIFTS quantitative protocol without the need for molar extinction coefficients'. In: *RSC Advances* 7.83 (2017), pp. 52604–52613. DOI: 10.1039/c7ra10699h (cit. on p. 30).

[65] P.J. Linstrom Mallard and W.G. *NIST Chemistry WebBook, NIST Standard Reference Database Number 69* (cit. on p. 31).

[66] Eiichi Kondoh et al. 'Removal of organic template of mesoporous organosilicate thin films using supercritical carbon dioxide fluids'. In: *Japanese Journal of Applied Physics* 56.7 (2017), pp. 5–8. DOI: 10.7567/JJAP.56.07KF02 (cit. on p. 31).

[67] B A Morrow and A J Mcfarlan. 'Surface Vibrational Modes of Silanol Groups on Silica'. In: *Journal of Physical Chemistry* 96.23 (1992), pp. 1395–1400. DOI: 10.1021/j100182a068 (cit. on p. 32).

[68] Silvia Bordiga et al. 'Probing zeolites by vibrational spectroscopies'. In: *Chem. Soc. Rev.* 44.20 (2015), pp. 7262–7341. DOI: 10.1039/C5CS00396B (cit. on p. 32).

[69] K Hadjiivanov et al. 'Effect of water on the reduction of NO x with propane on Fe-ZSM-5 . An FTIR mechanistic study'. In: *Catalysis Letters* 62.x (1999), pp. 35–40 (cit. on p. 35).

[70] Soran Shwan et al. 'Effect of thermal ageing on the nature of iron species in Fe-BEA'. In: *Catalysis Letters* 143.1 (2013), pp. 43–48. DOI: 10.1007/s10562-012-0940-z (cit. on p. 35).

[71] C. Hirose et al. 'Orientation Analysis by Simulation of Vibrational Sum Frequency Generation Spectrum: CH Stretching Bands of the Methyl Group'. In: *Journal of Physical Chemistry* 97(39) (1993), pp. 10064–10069. DOI: 10.1021/j100141a028 (cit. on p. 37).

[72] *NIST Chemistry WebBook*. http://https://webbook.nist.gov/chemistry/ (cit. on p. 39).

[73] A. G. Pelmenschikov et al. 'Mechanisms of methanol adsorption on silicalite and silica: IR spectra and ab-initio calculations'. In: *Journal of Physical Chemistry* 97.46 (1993), pp. 11979–11986. DOI: 10.1021/j100148a023 (cit. on p. 39).

[74] Sharelle M. Campbell, Xuan Zhen Jiang and Russell F. Howe. 'Methanol to hydrocarbons: Spectroscopic studies and the significance of extra-framework aluminium'. In: *Microporous and Mesoporous Materials* 29.1-2 (1999), pp. 91–108. DOI: 10.1016/S1387-1811(98)00323-0 (cit. on p. 39).

[75] Xueting Wang et al. 'Methanol Desorption from Cu-ZSM-5 Studied by in Situ Infrared Spectroscopy and First-Principles Calculations'. In: *Journal of Physical Chemistry C* 121.49 (2017), pp. 27389–27398. DOI: 10.1021/acs.jpcc.7b07067 (cit. on pp. 39, 40).

[76] Benjamin R. Wood et al. 'Methanol formation on Fe/Al-MFI via the oxidation of methane by nitrous oxide'. In: *Journal of Catalysis* 225.2 (2004), pp. 300–306. DOI: 10.1016/j.jcat.2004.04.010 (cit. on pp. 40, 42, 43).

[77] Ludmila Kubelková, Jana Nováková and Květa Nedomová. 'Reactivity of surface species on zeolites in methanol conversion'. In: *Journal of Catalysis* 124.2 (1990), pp. 441–450. DOI: 10.1016/0021-9517(90)90191-L (cit. on p. 40).

[78] Bernd Hunger et al. 'Adsorption of methanol on ZSM-5 zeolites'. In: *Langmuir* 13.23 (1997), pp. 6249–6254. DOI: 10.1021/la970615i (cit. on p. 40).

[79] Satoshi Kameoka et al. 'Reaction between N2O and CH4 over Fe ion-exchanged BEA zeolite catalyst: A possible role of nascent oxygen transients from N 2O'. In: *Physical Chemistry Chemical Physics* 5.15 (2003), pp. 3328–3333. DOI: 10.1039/b300562n (cit. on p. 42).

[80] Wan Zhen Liang et al. 'Density Functional Theory Investigations of the Direct Oxidation of Methane on an Fe-Exchanged Zeolite'. In: *Journal of Physical Chemistry B* 108.14 (2004), pp. 4362–4368. DOI: 10.1021/jp030929g (cit. on p. 43).

[81] Eva Roedel et al. 'On the local sensitivity of different IR techniques: Ba species relevant in NOx storage-reduction'. In: *Physical Chemistry Chemical Physics* 10.40 (2008), pp. 6190–6198. DOI: 10.1039/b808529c (cit. on p. 44).

Appendix

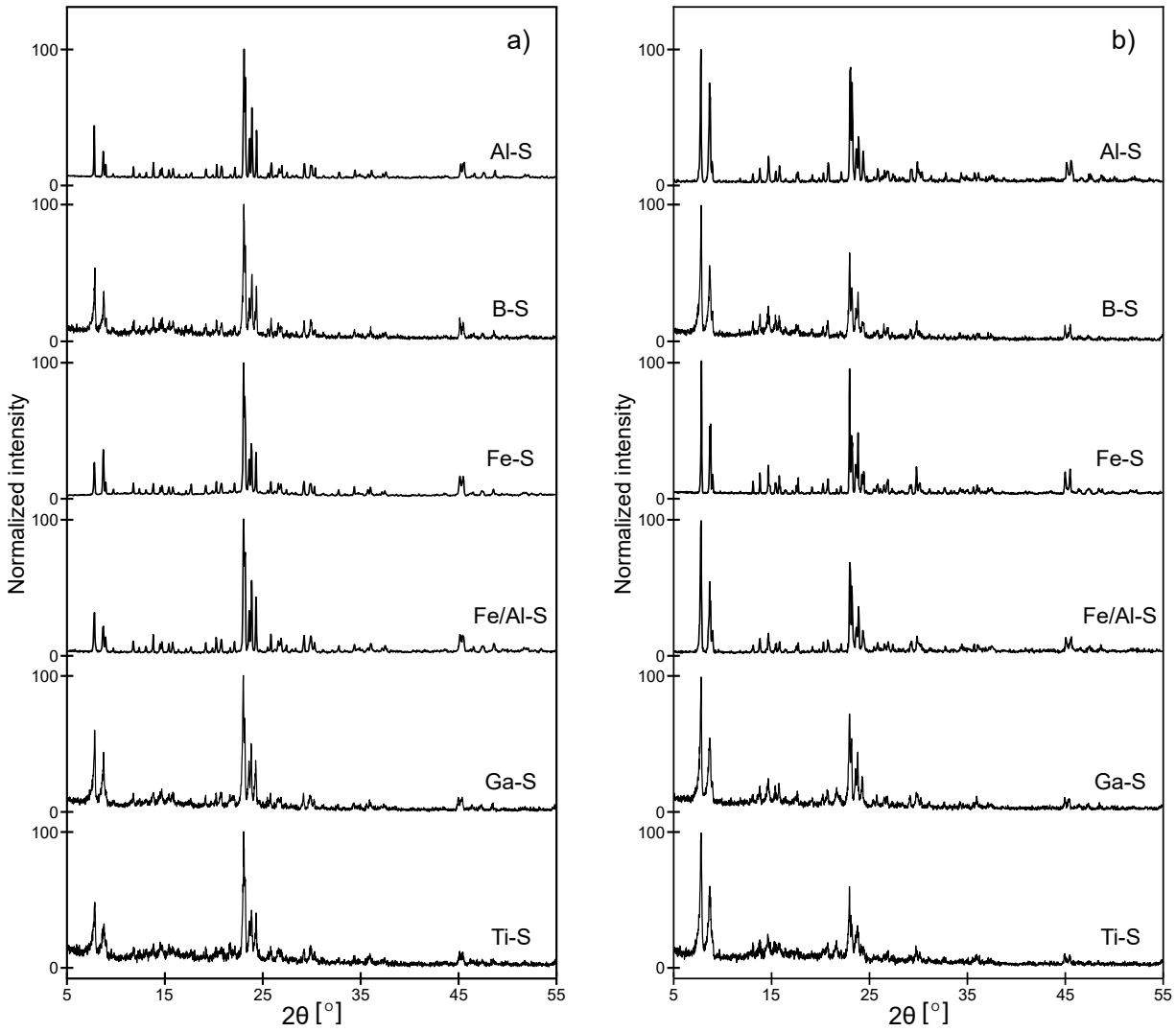

Figure A1: X-ray diffractograms of all samples a) before and b) after calcination.